



A vision-based autopilot for a miniature air vehicle: joint speed control and lateral obstacle avoidance

Julien Serres, D Dray, F. Ruffier, N. Franceschini

► To cite this version:

Julien Serres, D Dray, F. Ruffier, N. Franceschini. A vision-based autopilot for a miniature air vehicle: joint speed control and lateral obstacle avoidance. *Autonomous Robots*, 2008, 25 (1-2), pp.103-122. 10.1007/s10514-007-9069-0 . hal-01758721

HAL Id: hal-01758721

<https://amu.hal.science/hal-01758721>

Submitted on 6 Apr 2018

HAL is a multi-disciplinary open access archive for the deposit and dissemination of scientific research documents, whether they are published or not. The documents may come from teaching and research institutions in France or abroad, or from public or private research centers.

L'archive ouverte pluridisciplinaire **HAL**, est destinée au dépôt et à la diffusion de documents scientifiques de niveau recherche, publiés ou non, émanant des établissements d'enseignement et de recherche français ou étrangers, des laboratoires publics ou privés.

A vision-based autopilot for a miniature air vehicle: joint speed control and lateral obstacle avoidance

J. Serres · D. Dray · F. Ruffier · N. Franceschini

Received: 27 October 2006 / Accepted: 3 December 2007 / Published online: 22 December 2007
© Springer Science+Business Media, LLC 2007

Abstract In our project on the autonomous guidance of Micro-Air Vehicles (MAVs) in confined indoor and outdoor environments, we have developed a vision based autopilot, with which a miniature hovercraft travels along a corridor by automatically controlling both its speed and its clearance from the walls. A hovercraft is an air vehicle endowed with natural roll and pitch stabilization characteristics, in which planar flight control systems can be developed conveniently. Our hovercraft is fully actuated by two rear and two lateral thrusters. It travels at a constant altitude (~ 2 mm) and senses the environment by means of two lateral eyes that measure the right and left optic flows (OFs). The visuo-motor control system, which is called LORA III (Lateral Optic flow Regulation Autopilot, Mark III), is a *dual OF regulator* consisting of two intertwined feedback loops, each of which has its own OF set-point and controls the vehicle's translation in one degree of freedom (surge or sway). Our computer-simulated experiments show that the hovercraft can navigate along a straight or tapered corridor at a relatively high speed (up to 1 m/s). It also reacts to any major step perturbations in the lateral OF (provided by a moving wall) and to any disturbances caused by a tapered corridor. The minimalistic visual system (comprised of only 4 pixels) suffices for the hovercraft to be able to control both its clearance from the walls and its forward speed jointly, without ever measuring

speed and distance. The non-emissive visual sensors and the simple control system developed here are suitable for use on MAVs with a permissible avionic payload of only a few grams. This study also accounts *quantitatively* for previous ethological findings on honeybees flying freely in a straight or tapered corridor.

Keywords OF (optic flow) · Motion detection · Autopilot · MAV (micro-air vehicle) · Hovercraft · Urban canyon navigation · Insect flight · Biorobotics · Biomimetics · Bionics

Abbreviations

- LORA I Lateral Optic Flow Regulation Autopilot, Mark I, as described in Serres et al. (2006a). It includes a single optic flow regulator
LORA II Lateral Optic Flow Regulation Autopilot, Mark II, as described in Serres et al. (2006b). It includes two optic flow regulators with a common set-point
LORA III Lateral Optic Flow Regulation Autopilot, Mark III, as described in this paper. It includes two optic flow regulators, each with its own OF set-point

1 Introduction

Winged insects are able to navigate swiftly in unfamiliar environments by extracting visual information from their own motion. The *optic flow* (OF) is the apparent motion of the image of contrasting features projected onto the insect's retina. Insects rely on OF to avoid collisions (Collett 1980; Wagner 1982; Tammero and Dickinson 2002), to follow a corridor (Kirchner and Srinivasan 1989; Baird et al. 2005;

J. Serres (✉) · D. Dray · F. Ruffier · N. Franceschini
Biorobotics Dept., Movement and Perception Inst., CNRS / Univ.
of the Mediterranean, 163 avenue Luminy, 13288 Marseille cedex
09, France
e-mail: julien.serres@univmed.fr

F. Ruffier
e-mail: franck.ruffier@univmed.fr

N. Franceschini
e-mail: nicolas.franceschini@univmed.fr

Ruffier et al. 2007; Serres et al. 2007), and to cruise and land (Srinivasan et al. 1996), for example.

Kirchner and Srinivasan (1989) observed that honeybees flying through a narrow tunnel tend to maintain equidistance from the flanking walls. To explain this *centring response*, these authors hypothesized that the animal may balance the apparent motion of the images of the walls between their two eyes. In the field of robotics, many authors have made use of this ‘optic flow balance’ hypothesis in designing visually guided wheeled vehicles (Coombs and Roberts 1992; Duchon and Warren 1994; Santos-Victor et al. 1995; Dev et al. 1997; Weber et al. 1997; Carelli et al. 2002; Argyros et al. 2004; Hrabar et al. 2005; Humbert et al. 2007), or aerial vehicles (Hrabar et al. 2005; Griffiths et al. 2006), and simulating flying agents (Neumann and Bühlhoff 2001; Muratet et al. 2005) and hovercraft (Humbert et al. 2005). The ‘optic flow balance’ hypothesis has been tested mainly in corridors and urban canyons. Despite the success of the ‘optic flow balance’ hypothesis in robotics, new behavioural experiments have shown that honeybees actually do not necessarily centre when traversing a corridor (Ruffier et al. 2007; Serres et al. 2007). They may follow one of the two walls at a certain distance, and it remains to be shown whether and how they could generate this behaviour on the basis of OF sensing.

Honeybees flying through a narrow tapered corridor tend to keep their flight speed proportional to the local corridor width by regulating the image velocity (Srinivasan et al. 1996). Some authors tested wheeled robots in which the groundspeed was controlled by comparing the sum of the two lateral OFs with a reference value (Santos-Victor et al. 1995; Srinivasan et al. 1999; Argyros et al. 2004).

Based on the biorobotic approach developed at our laboratory over the past 20 years, several terrestrial and aerial vehicles based on OF have been constructed (Franceschini et al. 1992; Mura and Franceschini 1996; Viollet and Franceschini 1999, 2005; Netter and Franceschini 2002; Ruffier and Franceschini, 2003, 2005; Franceschini et al. 2007) or simulated (Mura and Franceschini 1994; Martin and Franceschini 1994; Serres et al. 2005, 2006a, 2006b). The LORA autopilot described here (LORA stands for Lateral Optic flow Regulation Autopilot) draws on former studies in which we designed the OCTAVE autopilot (OCTAVE stands for Optical flow based Control sysTem for Aerial VEHicles) enabling a Micro-Air Vehicle (MAV) to follow the terrain (Ruffier and Franceschini 2003, 2005; Franceschini et al. 2007). The LORA autopilot differs from OCTAVE in that LORA focuses on both issues of *automatic speed control* and *side wall avoidance*. We originally developed LORA I, which was a *heading control system* (Serres et al. 2005, 2006a) that could be applied to non-holonomic or underactuated vehicles. We then developed LORA II, which was a *forward-plus-side-slip control system* based on *two OF regulators*

with a common OF set-point (Serres et al. 2006b) that could be applied to holonomic and fully actuated vehicles. Our latest autopilot, called LORA III, consists of a *dual OF regulator* in which each regulator has its own OF set-point. LORA III regulates the OF by side and forward controls, according to the following principles:

- (i) the first *lateral OF regulator* adjusts the air vehicle’s lateral thrust (which determines the lateral speed V_y , i.e., the sway speed) so as to keep the lateral OF equal to the *sideways OF set-point*. The outcome is that the distance to the wall becomes proportional to the vehicle’s forward speed V_x which is defined in (ii): the faster the air vehicle travels, the further away from the walls it will be. The clearance from the walls will depend directly on the *sideways OF set-point*.
- (ii) the second *lateral OF regulator* adjusts the air vehicle’s forward thrust (which determines the forward speed V_x , i.e., the surge speed) so as to maintain the sum of the two (right and left) OFs equal to the *forward OF set-point*. The outcome is that the air-vehicle travels all the faster as the environment is less cluttered. The forward speed attained by the vehicle will depend directly on the *forward OF set-point*.

The miniature hovercraft we are working on (Fig. 1) is an advantageous ‘MAV’ in many ways. It makes no contact with the ground and ‘flies’ on a plane at a constant height of about 2 mm, which eliminates the need to implement an *altitude* control system on-board. A hovercraft is also endowed with inherent roll and pitch stabilization characteristics, which does away with the need to implement an *attitude* control system on-board. Besides, unlike wheeled robots, it can undergo disturbances on three degrees of freedom (such as those caused by headwind and sidewind, and the resulting side effects). LORA III computer-simulated experiments showed its excellent performances in straight and tapered corridors. With both types of corridor, the hovercraft managed to reach a safe forward speed at a safe clearance from the walls.

In Sect. 2, the simulation set-up used to test the LORA III *dual OF regulator* scheme implemented on our fully actuated hovercraft is described. In Sect. 3, the LORA III autopilot is described in detail. Section 4 deals with the theoretical steady state operating point reached by the LORA III autopilot in straight and tapered corridors. Section 5 details the tuning procedures for the controllers. Section 6 deals with the computer-simulated experiments carried out on our fully actuated hovercraft equipped with the LORA III autopilot. The results obtained show that LORA III enables the robot to perform various tasks such as *wall-following* and *centring* without having to switch abruptly from one behaviour to the other. In straight and tapered corridors, LORA III automatically adjusts the hovercraft’s forward speed to



Fig. 1 Sighted fully actuated hovercraft developed for testing the LORA III autopilot. Four ducted fans (GWS EDF-50, PMW-controlled DC motor CN12-RLC) drive the robot in the plane. The hovercraft is a retrofitted version of a miniature RC hovercraft (Taiyo Toy Ltd., Typhoon T-3: $0.36 \times 0.21 \times 0.14$ m). The robot is equipped with two lateral eyes looking at an angle of $\pm 90^\circ$ to the side, each of them driving a single OF sensor comprised of a pair of PIN photodiode. An additional brushless DC motor actuates the airbag turbine

the local width of the corridor, while keeping the robot at a safe distance from the walls, in much the same way as honeybees do in a similar situation. We also analyzed the autopilot's response to perturbations produced by one of the two side walls moving forwards or backwards and by a tapered corridor. It is concluded that the LORA III autopilot provides a simple, lightweight, low cost means of guiding a fully actuated aerial vehicle, while matching the behaviour of honeybees in similar environments.

2 Simulation set-up

All the present computer-simulated experiments were carried out on a standard PC equipped with the MatlabTM/Simulink software program at a sampling frequency of 1 kHz. This sampling frequency is the same as the sampling rate of the microcontroller installed onboard the LORA robot (Fig. 1). Our robotic simulations include: a dynamic hovercraft model (on the surge and sway axes), actuator saturations, the full optical transfer function of each lens/photoreceptor system, the complete OF sensory processing system (including its nonlinearities and the errors in the OF measurement), and the detailed interactions between the random patterns occurring on the walls and each photoreceptor.

2.1 Dynamic hovercraft model and mechanical design

A hovercraft can be said to be *holonomic in the plane* because it is free to move forwards or sideways and to turn

about its yaw axis. A hovercraft equipped with only two rear thrusters is said to be *underactuated*. Our hovercraft (Fig. 1), however, is a retrofitted version of a miniature RC hovercraft (Taiyo Toy Ltd., Typhoon T-3: $0.36 \times 0.21 \times 0.14$ m, based on the same robotic platform as that used by Seguchi and Ohtsuka 2003). It is *fully actuated* because in addition to the pair of rear thrusters providing forward motion (surge axis) and heading control (yaw axis) (Fig. 1), the vehicle is equipped with a pair of lateral thrusters generating independent side-slip motion (sway). The hovercraft's heading angle ψ with respect to the corridor axis, is kept at a reference value equal to zero:

$$\psi = 0. \quad (1)$$

In this study, the hovercraft's heading ψ is assumed to be stabilized along the X-axis of the corridor. This is achieved by implementing a heading lock system based on a micro-magnetic compass (Fig. 2a). This system is intended to compensate for any yaw disturbances by controlling the two rear thrusters *differentially*. Bees are likewise equipped with a heading lock system (based on a polarized light cue, von Frisch 1948), which makes the insect take an impressively straight course even in the presence of wind (Riley and Osborne 2001). Besides, the most common flight trajectories of flies have been found to consist of straight flight sequences interspersed with rapid turns termed *saccades* (Wagner 1986; Schilstra and van Hateren 1999). These ethological findings on the behavior of flying insects showed the existence of two distinct visuomotor mechanisms controlling insects' translations and rotations. Here we focus on the bio-inspired autopilot we designed, which may explain how a flying insect makes use of its two translational degrees of freedom in the plane. In this indoor study, where the hovercraft was not subjected to any wind, the groundspeed was taken to be equal to the airspeed. In the 2-D approximations used throughout this paper, the hovercraft's motion is defined by dynamic equations involving the *forward thrust* ($F_{Fwd} = F_{RT1} + F_{RT2}$) produced by the rear thrusters (left: RT1, right: RT2) and the *lateral thrust* ($F_{Side} = F_{LT1} - F_{LT2}$) produced by the lateral thrusters (left: LT1, right: LT2). In our simulation, the maximum forward speed is 2 m/s and the maximum side speed is 0.5 m/s. At such low speeds, the drag-versus-speed function can be linearized. The following equations referred to the center of gravity G define the dynamics of the simulated hovercraft (Fig. 2a):

$$m \cdot dV_x/dt + \zeta_x \cdot V_x = F_{RT1} + F_{RT2}, \quad (2a)$$

$$m \cdot dV_y/dt + \zeta_y \cdot V_y = F_{LT1} - F_{LT2}, \quad (2b)$$

where m (platform: 0.60 kg + batteries: 0.126 kg) is the mass of the hovercraft, and ζ_x and ζ_y are translational viscous friction coefficients along the X-axis and Y-axis, respectively. The hovercraft is both holonomic and fully actuated: each groundspeed component V_x ((2a) and (3a)) and

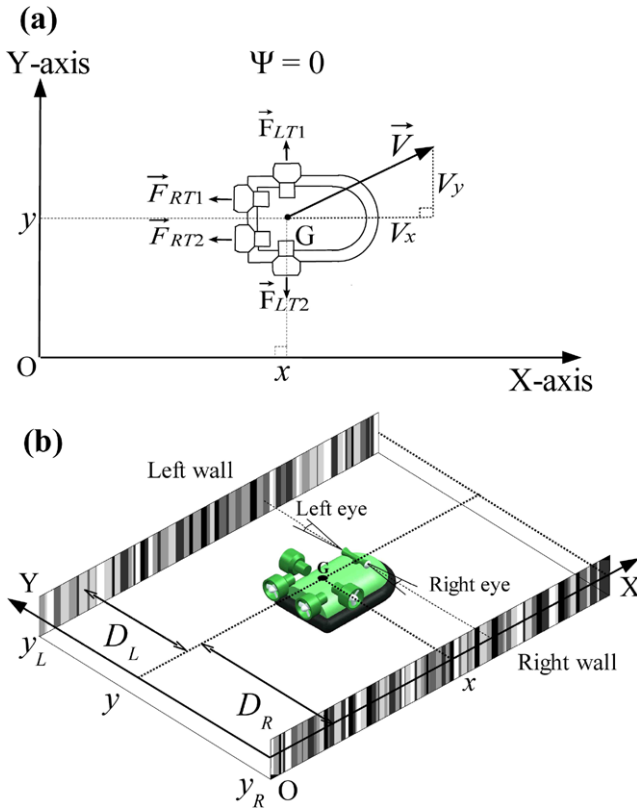


Fig. 2 **a** The hovercraft's groundspeed vector \vec{V} can be projected onto the corridor-fixed coordinate frame. Four thrusters allow the hovercraft to be *fully actuated*, and hence to control the three degrees of freedom in the plane independently. The forward speed V_x (on the surge axis) results from the total thrust ($F_{Fwd} = F_{RT1} + F_{RT2}$) exerted by the two rear thrusters. The side speed V_y (on the sway axis) results from the force exerted by the two lateral thrusters ($F_{Side} = F_{LT1} - F_{LT2}$). **b** Miniature hovercraft moving through an unknown textured corridor. The vehicle's heading is maintained along the X -axis (cf. (1)) by means of a heading lock system (based on a micro-magnetic compass) that compensates for any yaw disturbances by acting on the two rear thrusters *differentially*. The hovercraft is equipped with two lateral eyes looking at $\pm 90^\circ$ to the vehicle's main axis. The right and left walls of the corridor are lined with a random pattern of various grey vertical stripes. The angular velocities of these patterns depend linearly on the hovercraft's forward speed and nonlinearly on the distance from the walls (right: D_R and left: D_L)

V_y ((2b) and (3b)) can be controlled independently.

We equipped the hovercraft with four thrusters (ducted fan GWS EDF-50, DC motor CN12-RLC). Each ducted fan can produce a thrust of up to 0.72 N at 7.2 V, and the thrust is proportional to the voltage applied (Jin et al. 2004; <http://www.gws.com.tw/>). The propeller dynamics will be neglected here. The following linearized system of equations referred to the center of gravity G defines the dynamics of the simulated hovercraft as a function of the four control signals:

$$m \cdot dV_x/dt + \zeta_x \cdot V_x = K_T \cdot (u_{RT1} + u_{RT2}), \quad (3a)$$

$$m \cdot dV_y/dt + \zeta_y \cdot V_y = K_T \cdot (u_{LT1} - u_{LT2}), \quad (3b)$$

where K_T (0.10 N/V) is a simple gain that relates the thrust to the applied voltage, u_{RT1} and u_{RT2} are the forward control signals received by the rear thrusters (left: RT1, right: RT2), u_{LT2} and u_{LT1} are the side control signals received by the lateral thrusters (left: LT1, right: LT2).

2.2 Optic flow (OF) generated by the hovercraft's own motion

The hovercraft travels at a groundspeed vector \vec{V} over a flat surface along a corridor, the walls of which are lined with vertical stripes with random spatial frequency and contrast (Fig. 2b) that mimick a richly textured environment (Iida 2001; Ruffier and Franceschini 2003, 2005). The hovercraft is equipped with two lateral eyes placed opposite each other, i.e. looking at $\pm 90^\circ$ to the side. Since any rotations is compensated for (see Sect. 2.1), each eye of the moving vehicle receives a purely translational OF, which is the relative angular velocity of each stripe edge on the wall (Fig. 2b). The right and left OF, ω_R and ω_L , respectively, can be simply defined as follows (Fig. 3):

$$\omega_R = V_x/D_R, \quad (4)$$

$$\omega_L = V_x/D_L, \quad (5)$$

where V_x is the hovercraft's forward speed, D_R and D_L are the distances to the right and the left walls, respectively.

2.3 Eyes and optic flow sensors

A bio-inspired OF sensor was originally designed in 1986 (Blanes 1986; Franceschini et al. 1986). The principle underlying this electro-optical image velocity sensor was based on findings obtained at our laboratory on the common housefly's Elementary Motion Detectors (EMDs), by performing electrophysiological recordings on single neurons while applying optical microstimuli to two single photoreceptor cells within a single ommatidium (Franceschini 1985; Franceschini et al. 1989).

An OF sensor consists of a lens/photoreceptor assembly, including the two photoreceptors driving an EMD circuit. The OF sensor eye consists of just two photoreceptors (i.e., two pixels), the visual axes of which are separated by an interreceptor angle $\Delta\varphi = 4^\circ$. Each photoreceptor's angular sensitivity is given by a bell-shaped function, the acceptance angle $\Delta\rho$ (the angular width at half height) of which is also $\Delta\rho = 4^\circ$. The principle of the EMD circuit used in our studies has been described in previous papers (Blanes 1986; Franceschini et al. 1986; Viollet and Franceschini 1999; Ruffier et al. 2003). It is a nonlinear circuit driven by two photoreceptors, which works in five processing stages (Pudas et al. 2007; Aubépart and Franceschini 2007). The EMD output is a monotonic function of the OF of a contrasting

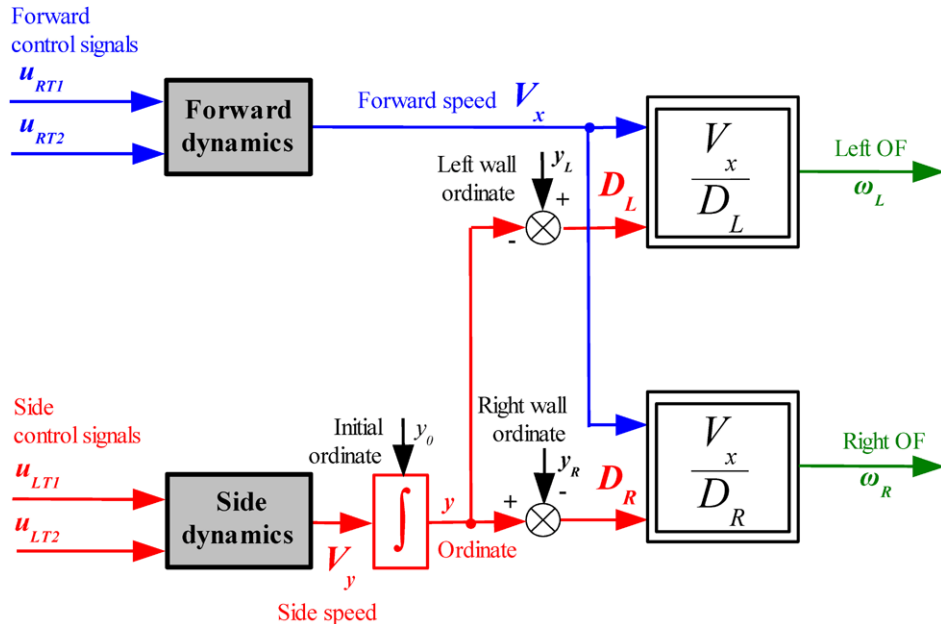


Fig. 3 Optic flow (OF) generated by the hovercraft's own motion. The forward control signal ($u_{RT1} + u_{RT2}$) commands the two rear thrusters (RT1 and RT2), and hence the hovercraft's forward dynamics (the surge dynamics). The side control signal ($u_{LT1} - u_{LT2}$) commands the two lateral thrusters (LT1 and LT2), and hence the hovercraft's side dynamics (the sway dynamics). The OF generated by the hovercraft's

own motion can be defined by the relative angular velocities of the wall patterns. The angular velocities depends nonlinearly on the distances from the walls (right: D_R and left: D_L) as shown by the two nested rectangles. The distances from the walls depend on the hovercraft's absolute ordinate y and the walls' absolute ordinates ($D_R = y - y_R$ and $D_L = y_L - y$). y_0 denotes the hovercraft's absolute initial position

edge within a 10-fold range (from $40^\circ/\text{s}$ to $400^\circ/\text{s}$) (Ruffier and Franceschini 2005; Pudas et al. 2007). Whenever the EMD circuit does not detect any new contrasting features, it holds the last measured value for a period of 0.5 s.

To simulate a photoreceptor's bell-shaped angular sensitivity, the output signal from each photoreceptor is computed at each time step by summing together all the grey level patterns present in its field of view (which covers approximately three $\Delta\rho$, i.e., 12°) and weighing the summation with a bottom truncated bell-shaped angular sensitivity function. During the computer-simulated experiments, the illuminance is kept constant so as to maintain the signal-to-noise ratio constant.

3 The LORA III autopilot

The hovercraft is controlled by an autopilot called LORA III (LORA stands for Lateral Optic flow Regulation Autopilot, Mark III), which involves multiple processing stages, as shown in the block diagrams in Figs. 3–5. LORA III actually consists of two visuomotor feedback loops: the *side control loop* and the *forward control loop*. Both loops work in parallel, each of them controlling its own translational degree of freedom (surge or sway) and possessing its own OF set-point. The coupling between the two feedback loops is illustrated, for example, by the fact that the overall feedforward

gain of the *side control loop* depends on the forward speed V_x (Fig. 4), which itself depends on the *forward control loop* (Fig. 5).

The most remarkable aspect of this dual control system is that neither the forward speed nor the distance to the walls need to be measured. The hovercraft reacts to any changes in the lateral OF by selectively adjusting the two orthogonal components V_x and V_y of its ground-speed vector \vec{V} (Fig. 2). The *side control loop* takes any increase in the *unilateral* OF to mean that the distance from the wall has decreased, and therefore adjusts the clearance via the sway dynamics. The *forward control loop* takes any increase in the *bilateral* OF to mean that an increase in the speed has occurred, and therefore adjusts the forward speed via the surge dynamics.

3.1 Bio-inspired side control system

The side control principle presented here is inspired by observations made on the flight behaviour of honeybees (Kirchner and Srinivasan 1989). These authors observed that honeybees tend to fly along the midline of a straight and narrow corridor. To explain this *centring response*, they hypothesised that '*bees maintained equidistance by balancing the velocities of the retinal images in the two eyes*' (Kirchner and Srinivasan 1989). When one of the walls was put

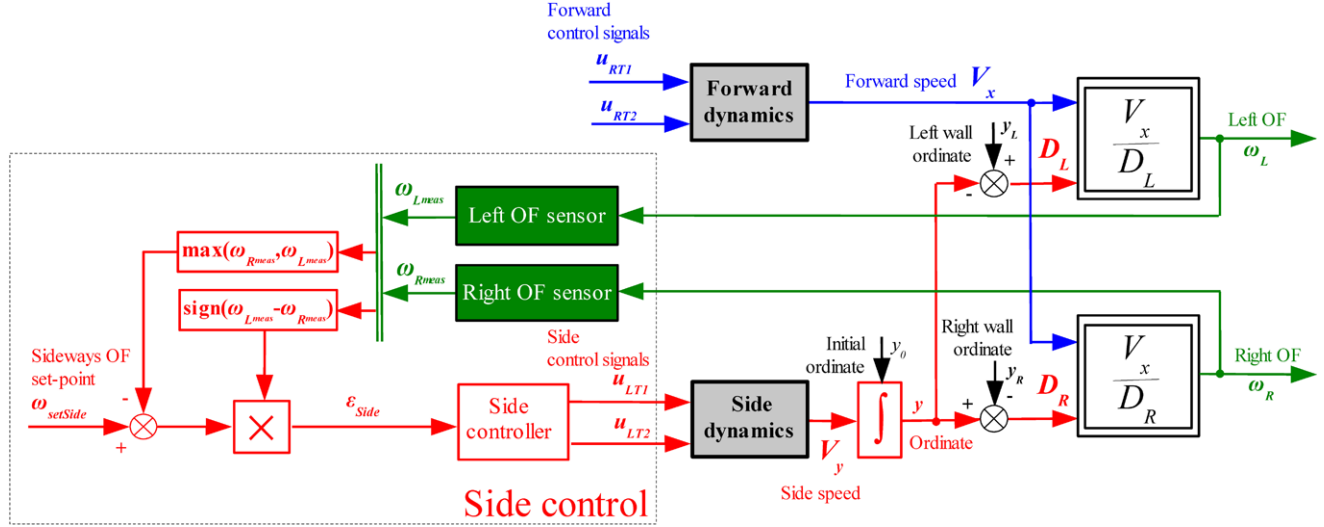


Fig. 4 The side control system is the first Optic Flow (OF) regulator in the LORA III dual OF regulator. Depending on the sign of the error signal ε_{Side} , one of the two lateral thrusters will be actuated. The side control signal ($u_{LT1} - u_{LT2}$) commands the side speed V_y . The forward speed V_x is an input parameter which is treated by the side control system like a simple feedforward gain. The right (left) lateral OF ω_R (ω_L) generated by the hovercraft's own motion depends on both the hovercraft's forward speed V_x and the distance from the right (left) wall

D_R (D_L) (see Fig. 3). The maximum value between the right (ω_{Rmeas}) and left (ω_{Lmeas}) OF measured is compared with a sideways OF set-point $\omega_{setSide}$, and the sign of the difference between the right and left lateral OFs measured will determine which of the two sides is followed. The wall on the right (right wall ordinate y_R), the wall on the left (left wall ordinate y_L), and the hovercraft's initial ordinate y_0 are treated by the visual feedback loop like disturbances (black arrows)

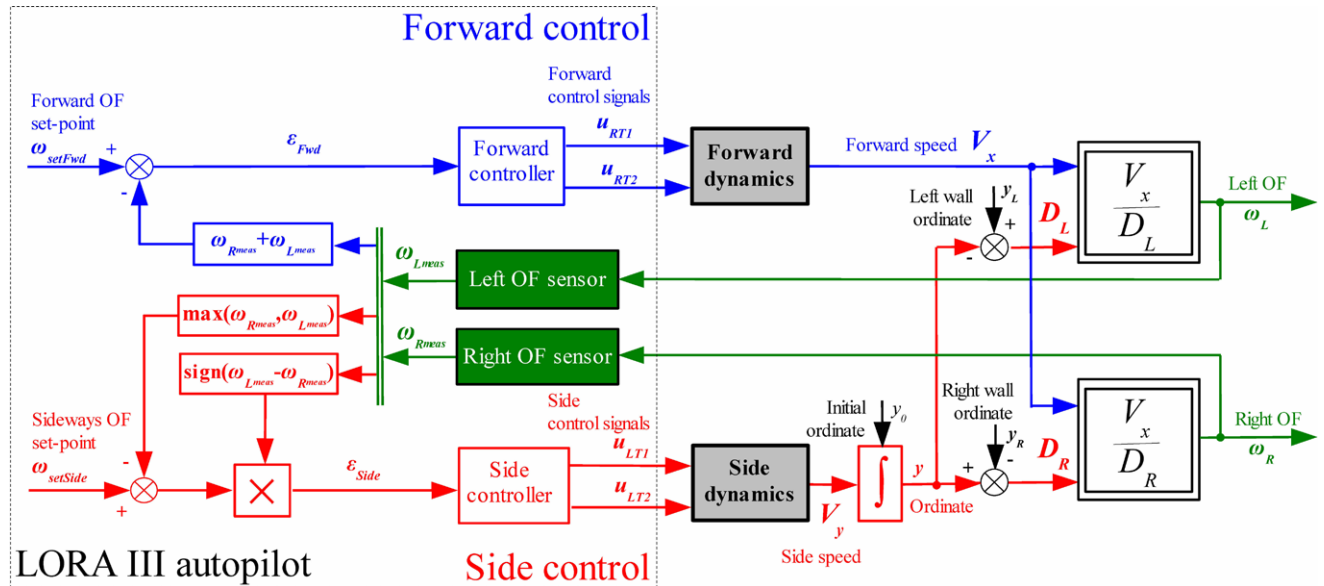


Fig. 5 The LORA III autopilot is based on two visual feedback loops working in parallel with their own optic flow set-point and their own degree of freedom controlled: the forward control system (blue upper loop) and the side control system (red bottom loop). The forward controller adjusts the forward thrust (which determines the hovercraft's forward speed V_x) on the basis of the sum of the right and left OFs measured (green blocks): $\omega_{Rmeas} + \omega_{Lmeas}$. This sum is compared with a forward OF set-point ω_{SetFwd} . The forward controller (PI) commands the forward motion (grey upper block) so as to minimize ε_{Fwd} . The

side controller (PD) adjusts the lateral thrust (which determines the hovercraft's side speed V_y) on the basis of the largest lateral OFs measured. This maximum value is compared with a sideways OF set-point $\omega_{SetSide}$, and the direction of avoidance is given by the sign of the difference between the left and right OFs measured. The side controller commands the side-slip motion (grey bottom block) so as to minimize the error ε_{Side} . The robot's initial ordinate y_0 , the right wall ordinate y_R and the left wall ordinate y_L are treated by LORA III like disturbances (black arrows)

into motion, bees flying in the same direction as the moving wall tended to fly closer to it, while bees flying in the opposite direction tended to fly farther away from it. The authors concluded that flying bees rely on the lateral image velocity to avoid collisions (Kirchner and Srinivasan 1989). We recently observed, however, that honeybees do not centre systematically in a wide corridor (Serres et al. 2007; Ruffier et al. 2007). Prompted to explain the wall-following behaviour we observed in bees, we came out with an explicit control system called the *side control feedback loop*.

The side control system is the first *OF regulator* (Fig. 4). This regulator is an improved version of the OCTAVE autopilot that was developed to ensure automatic ground avoidance in a rotorcraft (Ruffier and Franceschini 2003, 2005; Franceschini et al. 2007). The lateral OF regulator is based on a feedback signal that takes into account the OF provided by the two walls of the corridor. The feedback signal consists of the larger of the two OFs measured (left or right), $\max(\omega_{Lmeas}, \omega_{Rmeas})$, which corresponds to the nearest wall, $\min(D_L, D_R)$. This *OF regulator* was designed to keep the lateral OF constantly equal to a *sideways OF set-point* $\omega_{SetSide}$. The hovercraft then reacts to any deviation in the lateral OF from $\omega_{SetSide}$ by adjusting its lateral thrust, which determines the hovercraft's side speed V_y : this eventually leads to a change in the distance to the left (D_L) or right (D_R) wall. A sign function automatically selects the wall to be followed, and a maximum criterion is used to select the higher OF value measured between ω_{Rmeas} and ω_{Lmeas} . This value is then compared with the *sideways OF set-point* $\omega_{SetSide}$ (Fig. 4). In the steady state, the OF selected will therefore become equal to the *sideways OF set-point*, due to the integrator (transfer function $1/s$) that is naturally present in this loop (cf. (7)). The error signal ε_{Side} feeding the side controller is calculated as follows:

$$\begin{aligned} \varepsilon_{Side} = & \text{sign}(\omega_{Lmeas} - \omega_{Rmeas}) \\ & \times (\omega_{SetSide} - \max(\omega_{Lmeas}, \omega_{Rmeas})). \end{aligned} \quad (6)$$

From (3b), the dynamics $G_y(s)$ relating the hovercraft's ordinate y to the control signal $(u_{LT1} - u_{LT2})$ have a transfer function that approximates a first-order low-pass filter (with a time constant of 0.5 s) in series with an integrator (cf. (7)).

$$\begin{aligned} G_y(s) = & \frac{Y(s)}{(U_{LT1} - U_{LT2})(s)} = \frac{1}{s} \times \frac{\frac{K_T}{\zeta_y}}{1 + \frac{m}{\zeta_y}s} \\ = & \frac{1}{s} \times \frac{0.1}{1 + 0.5s}. \end{aligned} \quad (7)$$

A lead controller $C_y(s)$ was introduced into this feedback loop to increase the damping, thus improving the stability and enhancing the response dynamics (see Tuning Procedure in Sect. 5.1).

The control signal $(u_{LT1} - u_{LT2})$ arising from the side controller is limited so as to set the maximum side speed V_y at ± 0.5 m/s. The two side control signals are generated as follows:

1. if $\varepsilon_{Side} > 0 \Rightarrow u_{LT2} = 0$, the left thruster only is actuated, and the right one is off;
2. if $\varepsilon_{Side} < 0 \Rightarrow u_{LT1} = 0$, the right thruster only is actuated, and the left one is off.

The maximum of the two side control signals u_{LT1} and u_{LT2} is set at 5 V.

3.2 Bio-inspired forward control system

This guidance strategy was based on findings obtained on the flight behaviour of honeybees in a small *tapered corridor* lined with a periodic pattern of black and white vertical stripes (Srinivasan et al. 1996). The authors observed that when bees were centred upon entering the corridor, their flight speed tended to be proportional to the local width of the corridor: the insects slowed down as they approached the narrowest section and accelerated when the corridor widened beyond this point. The authors concluded that '*the speed of the flight is controlled by regulating the image velocity*' (Srinivasan et al. 1996).

The second *OF regulator* (Fig. 5, blue upper loop) is the forward control system. It is intended to hold the *sum* of the two lateral OFs measured ($\omega_{Rmeas} + \omega_{Lmeas}$) constant and equal to a *forward OF set-point* ω_{SetFwd} by adjusting the forward thrust, which will determine the hovercraft's forward speed V_x . At a given corridor width, any increase in the sum of the two lateral OFs is assumed here to result from the hovercraft's acceleration. This control scheme thus automatically ensures a 'safe forward speed' that is commensurate with the local corridor width. The sum of the two OFs measured is compared with a *forward OF set-point* ω_{SetFwd} , and the error signal ε_{Fwd} (the input to the forward controller in Fig. 5) is calculated as follows:

$$\varepsilon_{Fwd} = \omega_{SetFwd} - (\omega_{Rmeas} + \omega_{Lmeas}). \quad (8)$$

The model $G_{V_x}(s)$ for the dynamics of our hovercraft (from (3a)), which relates the forward speed V_x to the forward control signal $u_{RT1} + u_{RT2}$ (Fig. 2), is described by a first order low-pass filter with a time constant of 0.5 s (cf. (9)):

$$G_{V_x}(s) = \frac{V_x(s)}{(U_{RT1} + U_{RT2})(s)} = \frac{\frac{K_T}{\zeta_x}}{1 + \frac{m}{\zeta_x}s} = \frac{0.1}{1 + 0.5s}. \quad (9)$$

A proportional-integral (PI) controller was introduced into the feedback loop to improve the closed-loop dynamics and to reach a zero steady state error (see Tuning Procedure in Sect. 5.2).

The forward control signal $u_{RT1} + u_{RT2}$ was limited so as to set the maximum forward speed V_x at 2 m/s. The maximum of the two forward control signals u_{RT1} and u_{RT2} is set at 10 V.

4 Theoretical steady state analysis

4.1 The steady state operating point in a straight corridor

In the following discussion, the LORA III autopilot is assumed to have reached the steady state ($t = \infty$). That is, the hovercraft is travelling at a forward speed $V_{x\infty}$ at a distance $D_{R\infty} = y_\infty$ from the right wall. The autopilot strives at all time to make the right OF equal to the *sideways OF set-point* $\omega_{SetSide}$ (see Sect. 3.1), while making the sum of the two lateral OFs equal to the *forward OF set-point* ω_{SetFwd} (see Sect. 3.2). The steady state operating point of the hovercraft ($V_{x\infty}, y_\infty$) can be defined as follows:

In the steady state:

$$\begin{cases} \omega_{SetFwd} = \omega_{R\infty} + \omega_{L\infty} \\ \omega_{SetSide} = \omega_{R\infty} \end{cases}$$

$$\Leftrightarrow \begin{cases} \omega_{SetFwd} = \frac{V_{x\infty}}{D_{R\infty}} + \frac{V_{x\infty}}{D_{L\infty}} & \text{from (4) and (5),} \\ \omega_{SetSide} = \frac{V_{x\infty}}{D_{R\infty}} & \text{from (4)} \end{cases} \quad (10a)$$

$$\Leftrightarrow \begin{cases} \omega_{SetFwd} = \frac{V_{x\infty}}{D_{R\infty}} + \frac{V_{x\infty}}{D_{L\infty}} & \text{from (4)} \\ \omega_{SetSide} = \frac{V_{x\infty}}{D_{R\infty}} & \text{from (4)} \end{cases} \quad (10b)$$

From this, we can derive the final operating point of the hovercraft ($V_{x\infty}, y_\infty$), as follows:

$$\begin{cases} V_{x\infty} = \frac{\omega_{SetSide} \cdot (\omega_{SetFwd} - \omega_{SetSide})}{\omega_{SetFwd}} \cdot D, \\ y_\infty = D_{R\infty} = \frac{\omega_{SetFwd} - \omega_{SetSide}}{\omega_{SetFwd}} \cdot D, \quad y_\infty \in [0, \frac{D}{2}], \\ D = D_{R\infty} + D_{L\infty}, \quad \text{where } D \text{ is the corridor width.} \end{cases} \quad (11)$$

This result has three important consequences:

- Both the steady state speed $V_{x\infty}$ and the steady state ordinate y_∞ can be seen to be proportional to the corridor width D . If the corridor is twice as large, the robot will automatically drive at twice the speed with twice the clearance from the wall. Conversely, if the corridor is half as wide, the robot will automatically drive at half speed and at half the clearance from the wall.
- If the *sideways OF set-point* $\omega_{SetSide}$ is larger than half the value of the *forward OF set-point* ω_{SetFwd} (i.e., $\omega_{SetSide} > \omega_{SetFwd}/2$), the hovercraft will reach a final ordinate y_∞ (cf. (11)) which is smaller than half the value of the corridor width. This means that it will keep close to one wall, thus generating *wall-following behaviour*.
- By contrast, if the *sideways OF set-point* $\omega_{SetSide}$ is smaller than half the value of the *forward OF set-point* ω_{SetFwd} (i.e., $\omega_{SetSide} < \omega_{SetFwd}/2$), the hovercraft will not be able to reach the final ordinate y_∞ predicted by (11) without causing a change in sign in the error signal ε_{Side}

(cf. (6)). As a result, the hovercraft will keep maintaining the OF value at $\omega_{SetFwd}/2$. It will navigate along the midline of the corridor, thus showing *centring behaviour*.

It is noteworthy that the LORA III autopilot enables the hovercraft to *control* both its forward speed and its distance from the walls without actually measuring any of these two variables. Besides, at a given *forward OF set-point* and a given *sideways OF set-point*, the hovercraft's final 'operating point' (as defined by its speed and its distance from the walls) depends only on the corridor width D (which is also unknown onboard the hovercraft at all times).

We now examine the effect of two types of perturbation that can affect the OFs measured: an unilateral OF step perturbation introduced by a moving wall and a bilateral OF disturbance introduced by a tapered corridor.

4.2 The steady state operating point in the case of an OF step perturbation introduced by a moving wall

Here we focus on the robustness of the LORA III autopilot to OF step perturbations. The latter are simulated by making the robot suddenly encounter a moving wall on one side. If the speed of the wall pattern is denoted V_p , the robot's relative speed with respect to the moving wall can be defined by $V_x - V_p$. This relative speed makes the robot shift towards or away from the moving wall. The contrast pattern speed V_p on the *right* wall is treated by LORA III like an 'output perturbation' that affects both loops (Fig. 6). The linearized block diagrams Fig. 6a, b show the point at which this perturbation is applied to the two control loops.

The perturbation can be defined as follows:

In the steady state:

$$\begin{cases} \omega_{SetFwd} = \omega_{R\infty} + \omega_{L\infty} \\ \omega_{SetSide} = \omega_{R\infty} \end{cases}$$

$$\Leftrightarrow \begin{cases} \omega_{SetFwd} = \frac{V_{x\infty} - V_p}{D_{R\infty}} + \frac{V_{x\infty}}{D_{L\infty}}, \\ \omega_{SetSide} = \frac{V_{x\infty} - V_p}{D_{R\infty}}. \end{cases} \quad (12a)$$

$$\Leftrightarrow \begin{cases} \omega_{SetFwd} = \frac{V_{x\infty} - V_p}{D_{R\infty}} + \frac{V_{x\infty}}{D_{L\infty}}, \\ \omega_{SetSide} = \frac{V_{x\infty} - V_p}{D_{R\infty}}. \end{cases} \quad (12b)$$

The final operating point of the hovercraft ($V_{x\infty}, y_\infty$) can therefore now be expressed as follows:

$$\begin{cases} V_{x\infty} = \frac{\omega_{SetSide} \cdot (\omega_{SetFwd} - \omega_{SetSide})}{\omega_{SetFwd}} \cdot D + \frac{(\omega_{SetFwd} - \omega_{SetSide})}{\omega_{SetFwd}} \cdot V_p, \\ y_\infty = D_{R\infty} = \frac{\omega_{SetFwd} - \omega_{SetSide}}{\omega_{SetFwd}} \cdot D - \frac{1}{\omega_{SetFwd}} \cdot V_p, \\ D = D_{R\infty} + D_{L\infty}, \quad \text{where } D \text{ is the corridor width.} \end{cases} \quad (13)$$

Clearly, the OF step perturbation introduced by a moving wall causes a shift in the final operating point ($V_{x\infty}, y_\infty$) of the hovercraft (cf. (13)) in comparison with that computed by (11).

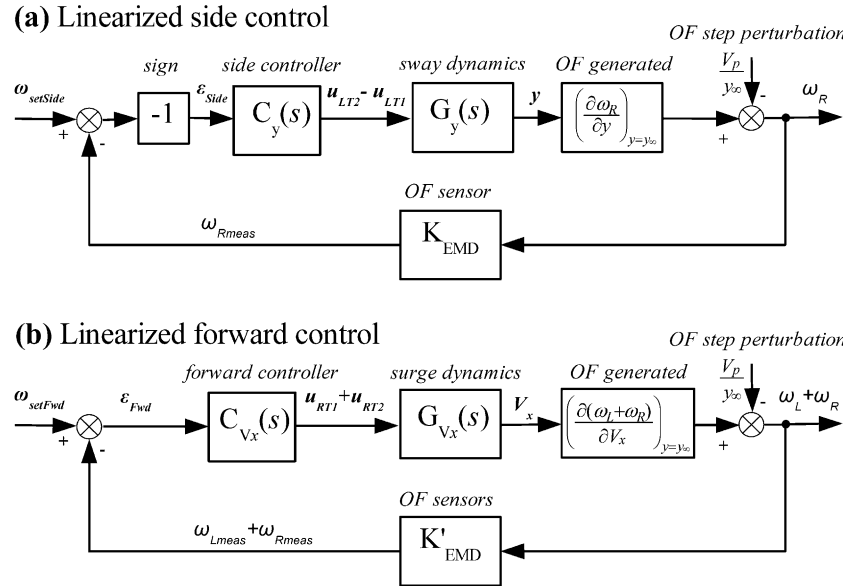


Fig. 6 Tuning procedure for the controllers $C_y(s)$ and $C_{Vx}(s)$. **a** Linearization of the side control system around the sideways OF set-point $\omega_{setSide} = 230^\circ/\text{s}$ assuming that the hovercraft is following the right wall ($\omega_{Rmeas} > \omega_{Lmeas}$), as attested by the function $\text{sign}(\omega_{Lmeas} - \omega_{Rmeas}) = -1$. The change in the right OF, ω_R , generated by the hovercraft's sideways motion along the Y -axis is $(\partial\omega_R/\partial y) = -V_x/y^2$ (by differentiating (4)) which is equal to $-\omega_{setSide}/y_\infty$ around the regulated operating point $\omega_{setSide}$ (y_∞ is the hovercraft's steady state ordinate, see Sect. 4.1 for details). The OF sensor is also linearized, and its local sensitivity is $K_{EMD} = (\partial\omega_{Rmeas}/\partial\omega_R) = 0.189 \text{ V}/(\text{rad/s})$ around $\omega_{setSide}$ ($230^\circ/\text{s}$). The OF sensor measures OF with greater sensitivity at low than high OF ($0.073 \text{ V}/(\text{rad/s}) < K_{EMD} < 1.202 \text{ V}/(\text{rad/s})$

4.3 The steady state operating point in the case of non-constant OF disturbance introduced by a tapered corridor

The lateral OF is here assumed to be *regulated* (i.e., maintained constant) along the whole tapered corridor. Under this condition, LORA III ensures that:

- (i) one of the two lateral OF (the right one, for instance) will be equal to the *sideways OF set-point* $\omega_{SetSide}$ (see Sect. 3.1).
- (ii) the sum of the two lateral OFs will be equal to the *forward OF set-point* ω_{SetFwd} in all circumstances and at all times (see Sect. 3.2).

The hovercraft's instantaneous forward speed $V_x(t)$ can be determined as follows:

At any time t :

$$\begin{cases} \omega_{SetFwd} = \omega_R(t) + \omega_L(t) \\ \omega_{SetSide} = \omega_R(t) \end{cases}$$

$$\Leftrightarrow \begin{cases} \omega_{SetFwd} = \frac{V_x(t)}{D_R(t)} + \frac{V_x(t)}{D_L(t)} & \text{from (4) and (5),} \\ \omega_{SetSide} = \frac{V_x(t)}{D_R(t)} & \text{from (4).} \end{cases} \quad (14a) \quad (14b)$$

within the 10-fold range from $40^\circ/\text{s}$ to $400^\circ/\text{s}$). In some experiments, the speed of the moving wall V_p acted as a step perturbation of the $V_p/y_\infty = \pm 115^\circ/\text{s}$ OF value. **b** Linearization of the forward control system around the forward OF set-point $\omega_{SetFwd} = 300^\circ/\text{s}$. The change in the sum of two lateral OF generated ($\omega_L + \omega_R$) by the hovercraft's forward motion along the X -axis is $\partial(\omega_L + \omega_R)/\partial V_x = 1/D_R + 1/D_L$ (by differentiating the sum of (4) and (5)), which is a simple feedforward gain independent of the forward speed V_x . The two lateral OF sensors operate at two distinct regulated values ($230^\circ/\text{s}$ and $70^\circ/\text{s}$): this requires taking a mean sensitivity K'_{EMD} of the two OF sensors that corresponds to the sensitivity of the OF sensor at $110^\circ/\text{s}$

Hence we can derive the instantaneous forward speed $V_x(t)$, as follows:

$$\begin{cases} V_x(t) = \frac{\omega_{SetFwd} \cdot (\omega_{SetFwd} - \omega_{SetSide})}{\omega_{SetFwd}} \cdot D(t), \\ D(t) = D_R(t) + D_L(t), \\ \text{with } D(t) \text{ the local corridor width.} \end{cases} \quad (15)$$

The instantaneous forward speed $V_x(t)$ turns out to be proportional to the current corridor width D at all times (cf. (15)). The tapered corridor is treated by the LORA III autopilot (Fig. 6b) like a ‘non-constant disturbance’, since it causes a linear change in the left and right wall ordinates y_L and y_R as a function of the distance x travelled. This makes the hovercraft respond by decreasing (or increasing) its forward speed *linearly* with the distance travelled. The local corridor width D can be expressed as a function of the tapering angle α (see Fig. 13a), as follows:

$$D(x) = y_L(x) - y_R(x) = y_{Lo} - y_{Ro} + 2 \cdot \tan(\alpha) \cdot x \quad (16)$$

According to (15) and (16), the forward speed $V_x(x)$ will be proportional to the distance travelled x :

$$\left\{ \begin{array}{l} V_x(x) = K(\alpha) \cdot x + V_{x_0}, \\ K(\alpha) = 2 \cdot \tan(\alpha) \cdot \frac{\omega_{SetSide} \cdot (\omega_{SetFwd} - \omega_{SetSide})}{\omega_{SetFwd}}, \end{array} \right. \quad (17a)$$

$$\left\{ \begin{array}{l} V_x(x) = K(\alpha) \cdot x + V_{x_0}, \\ K(\alpha) = 2 \cdot \tan(\alpha) \cdot \frac{\omega_{SetSide} \cdot (\omega_{SetFwd} - \omega_{SetSide})}{\omega_{SetFwd}}, \\ V_{x_0} = (y_{L_0} - y_{R_0}) \cdot \frac{\omega_{SetSide} \cdot (\omega_{SetFwd} - \omega_{SetSide})}{\omega_{SetFwd}}. \end{array} \right. \quad (17b)$$

A plot of dx/dt versus x will give a linear function (cf. 17a) in the *phase plane* (x , dx/dt). Upon differentiating (17a), the forward speed obtained is the solution of the following first-order differential equation:

$$\frac{dV_x(t)}{dt} + K(\alpha) \cdot V_x(t) = 0. \quad (18)$$

This means that the speed will vary as an exponential function of time (cf. (19)) with a *time constant* $\tau(\alpha)$ (cf. (20)) that depends on the tapering angle α as follows:

$$V_x(t) = V_x(t_0) \cdot e^{\text{sign}(\alpha) \cdot (t - t_0)/\tau(\alpha)}, \quad (19)$$

$$\begin{aligned} \tau(\alpha) &= \frac{1}{|K(\alpha)|}, \\ \tau(\alpha) &= \frac{\omega_{SetFwd}}{2 \cdot \tan |\alpha| \cdot \omega_{SetSide} \cdot (\omega_{SetFwd} - \omega_{SetSide})}. \end{aligned} \quad (20)$$

Thus, without any knowledge of the tapering angle α , the hovercraft is bound to slow down as an exponential function of time (cf. (19)) when it enters a narrowing section ($\alpha < 0$), and to accelerate as an exponential function of time when the section widens again ($\alpha > 0$). $\tau(\alpha)$ is the time constant (cf. (20)) of the visual closed loop in the tapered corridor. In a straight corridor ($\alpha = 0$), the hovercraft's forward speed will remain constant, as computed with (11).

5 Tuning procedures for the controllers

The side and forward controllers are tuned by linearizing the two visual feedback loops around the regulated operating point of each OF regulator (Fig. 6).

The forward ($\omega_{SetFwd} = 300^\circ/\text{s}$) and sideways ($\omega_{SetSide} = 230^\circ/\text{s}$) OF set-points are chosen with a view to reaching a safe forward speed $V_{x\infty} = 1 \text{ m/s}$ and a safe distance to the nearest wall $y_\infty = D_{R\infty} = 0.23 \text{ m}$ in the steady state, at a given corridor width of 1 m (cf. (11)), in much the same way as honeybees do in similar situations (Serres et al. 2007; Ruffier et al. 2007).

5.1 Tuning procedure for the side controller

A lead controller $C_y(s)$ is introduced into the side control system to improve the stability and enhance its response dynamics. The natural integrator that relates the robot's ordinate y to its side speed V_y makes the side control system reach a zero steady state error.

The side control feedback loop is linearized assuming the robot is following, for instance, the right wall at the sideways OF set-point (Fig. 6a). The open-loop transfer function $T_{side open-loop}(s)$ can be written as follows:

$$T_{side open-loop}(s) = -C_y(s) \cdot G_y(s) \cdot \frac{\partial \omega_R}{\partial y} \cdot K_{EMD},$$

$$\left(\frac{\partial \omega_R}{\partial y} \right)_{y=y\infty} = -\frac{\omega_{setSide}}{y_\infty} = -17.204 \text{ (rad/s/m)},$$

$K_{EMD} = 0.189 \text{ V/(rad/s)}$ corresponding to the OF sensor sensitivity at the OF value of $230^\circ/\text{s}$.

The lead controller $C_y(s)$ (cf. (21)) is tuned to reach a phase margin of 45° and a crossover frequency of 4 rad/s (0.64 Hz).

$$C_y(s) = \frac{(U_{LT1} - U_{LT2})(s)}{\varepsilon_{Side}(s)} = 10 \times \frac{1 + 1.5s}{1 + 0.5s}. \quad (21)$$

5.2 Tuning procedure for the forward controller

The forward OF set-point ω_{SetFwd} ($300^\circ/\text{s}$) has to be set as follows: $\omega_{SetFwd} = \omega_R + \omega_L = 2.21 \text{ V}$ ($230^\circ/\text{s}$) + 1.07 V ($70^\circ/\text{s}$) = 3.28 V . We linearize the forward control feedback loop around the forward OF set-point (Fig. 6b). The linearized forward open-loop transfer function $T_{FwdOpen-Loop}(s)$ can be written as follows:

$$T_{FwdOpen-Loop}(s) = C_{V_x}(s) \cdot G_{V_x}(s) \cdot \frac{\partial(\omega_L + \omega_R)}{\partial V_x} \cdot K'_{EMD},$$

$$\left(\frac{\partial(\omega_L + \omega_R)}{\partial V_x} \right)_{y=y\infty} = \frac{D_{L\infty} + D_{R\infty}}{D_{L\infty} \cdot D_{R\infty}} = 5.647 \text{ rad/s}$$

with a corridor width $D_{L\infty} + D_{R\infty} = 1 \text{ m}$ and $y_\infty = D_{R\infty} = 0.23 \text{ m}$, $K'_{EMD} = 0.557 \text{ V/(rad/s)}$ corresponding to the mean sensitivity of the OF sensors for a right OF value of $230^\circ/\text{s}$ and a left OF value of $70^\circ/\text{s}$.

The proportional-integral (PI) controller $C_{V_x}(s)$ (cf. (22)) is tuned to cancel the dominant (aeromechanical) pole of the hovercraft and to reduce the forward time constant computed in the closed-loop by a factor of 1.57. The integral action is introduced to cancel the steady state error.

$$C_{V_x}(s) = \frac{(U_{RT1} + U_{RT2})(s)}{\varepsilon_{Fwd}(s)} = 10 \times \frac{1 + 0.5s}{s}. \quad (22)$$

In what follows, we test the LORA III *dual OF regulator* in a straight corridor where the hovercraft starts at various initial ordinates y_0 , as well as in a nonstationary corridor where part of one wall moves at the speed V_p . The moving wall (Fig. 6) acts as an *OF step perturbation* on the LORA III. Lastly, the hovercraft is tested in a tapered corridor that subjects the LORA III autopilot to a *non-constant disturbance*.

6 Simulation Results

6.1 Automatic lateral positioning in a straight corridor

The simulation set-up was presented in detail in Sect. 2. The simulated visual environment here is a straight 3-meter long, 1-meter wide corridor with randomly contrasting walls. The right and left walls are lined with a random pattern of various grey vertical stripes covering a 1-decade contrast range (from 4% to 38%) and a 1.1-decade angular frequency range (from 0.068 c° to 0.87 c° reading from the corridor midline). No special steps were taken to make the two opposite patterns mirror-symmetric.

Figure 7a shows three simulated trajectories resulting from the LORA III *dual OF regulator* scheme (Fig. 5). It can be seen from this figure that the hovercraft navigates safely, regardless of its initial ordinate y_0 at the entrance to the corridor. In these trajectories where the *sideways OF set-point* $\omega_{SetSide} = 230^\circ/\text{s}$ is larger than half the value of the *forward OF set-point* ($\omega_{SetFwd} = 300^\circ/\text{s}$), i.e., $\omega_{SetSide} > \omega_{SetFwd}/2$, the hovercraft can be seen to adopt *wall-following behaviour* (as predicted in Sect. 4.1): it follows the right or the left wall, depending on its initial ordinate y_0 . In the three simulated cases (Fig. 7a), the hovercraft generates a steady state clearance of 0.25 m from either wall (left wall: squares, and crosses; right wall: full dots) and reaches a ‘safe forward speed’ of $V_{x\infty} = 1 \text{ m/s}$ (Fig. 7b). The final operating point is close to that calculated from (11): taking $\omega_{SetFwd} = 300^\circ/\text{s}$ and $\omega_{SetSide} = 230^\circ/\text{s}$, a 1-meter wide ($D = 1 \text{ m}$) corridor leads to final operating values ($V_{x\infty} = 0.94 \text{ m/s}$; $y_\infty = 0.23 \text{ m}$).

The hovercraft can be seen to follow either the right or the left wall, depending on the sign of the error signal ε_{side} (cf. (6)). The hovercraft’s initial ordinate y_0 is treated by the LORA III autopilot (Fig. 5) as a disturbance, which is rejected by the *dual OF regulator*. It can be seen from Fig. 7d, f that both the sum and the maximum value of the two lateral OFs reach their respective OF set-point.

It can be seen from Fig. 8 that when the *sideways OF set-point* $\omega_{SetSide}$ is smaller than half the value of the *forward OF set-point* ω_{SetFwd} (i.e., $\omega_{SetSide} < \omega_{SetFwd}/2$), the OFs measured (ω_{Rmeas} or ω_{Lmeas}) never reach $\omega_{SetSide}$. The hovercraft is bound to centre between the two walls (as predicted in Sect. 4.1), oscillating about the midline due to the changing sign of the error signal ε_{side} (cf. (6)). (One way of cancelling these repeated changes in sign might consist in substituting the sign function for a hysteresis comparator.) The OF is minimum along the midline of the corridor but cannot become smaller than $150^\circ/\text{s}$ (half the value of ω_{SetFwd}). The error signal ε_{side} (Figs. 4, 5) is therefore also minimum along the midline. The hovercraft can be seen to reach the *same* forward speed of $V_{x\infty} = 1.3 \text{ m/s}$ (Fig. 8b) in all three cases, although these feature *different* values of

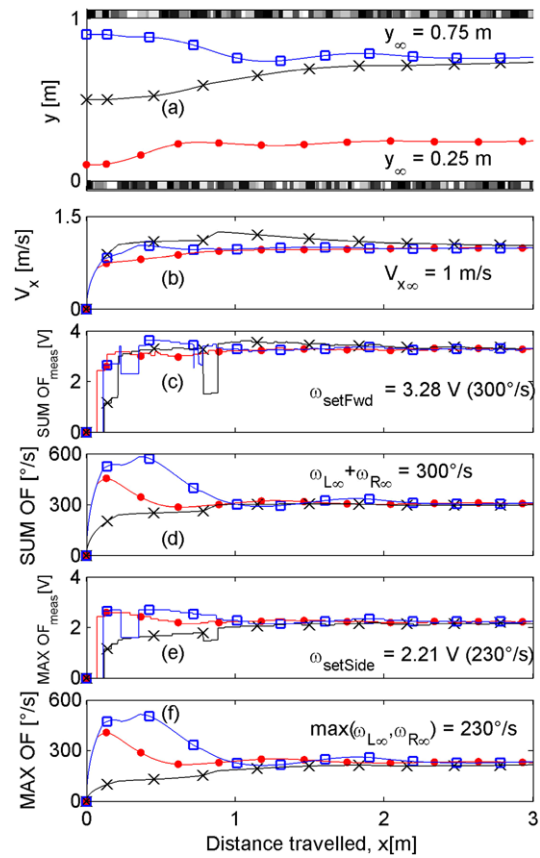


Fig. 7 Automatic wall-following behaviour as a function of the initial condition y_0 (Marks on trajectories indicate the hovercraft position at 0.3-second intervals). **a** Three simulated trajectories of the hovercraft moving to the right in a straight corridor at a forward OF set-point $\omega_{SetFwd} = 3.28 \text{ V}$ (i.e., $300^\circ/\text{s}$) and a sideways OF set-point $\omega_{SetSide} = 2.21 \text{ V}$ (i.e., $230^\circ/\text{s}$), starting at different initial positions (squares: $y_0 = 0.90 \text{ m}$, crosses: $y_0 = 0.50 \text{ m}$, full dots: $y_0 = 0.10 \text{ m}$). In the steady state, the clearance from the nearest wall reaches 0.25 m in the three simulated cases. **b** Forward speed profiles corresponding to the trajectories shown in (a). In the steady state, the forward speed reaches $V_{x\infty} = 1 \text{ m/s}$ in the three simulated cases. **c** Sum of the two lateral OFs measured ($\omega_{Lmeas} + \omega_{Rmeas}$) by the OF sensors corresponding to the trajectories shown in (a). In the steady state, this sum of the lateral OFs measured reaches the forward OF set-point $\omega_{SetFwd} = 3.28 \text{ V}$ in the three simulated cases. **d** Sum of the two lateral OFs ($\omega_L + \omega_R$) generated by the hovercraft’s own motion reaches $300^\circ/\text{s}$, which corresponds to the output of the forward control system. **e** Maximum value of the two lateral OFs measured $\max(\omega_{Lmeas}, \omega_{Rmeas})$ by the OF sensors corresponding to trajectories shown in (a). In the steady state, this maximum value reaches the sideways OF set-point $\omega_{SetFwd} = 2.21 \text{ V}$ in the three simulated cases. **f** Maximum value measured by the two lateral OFs $\max(\omega_L, \omega_R)$ generated by the hovercraft’s own motion (computed with (4) plus (5)) corresponding to the trajectories shown in (a). In the steady state, this maximum value reaches $230^\circ/\text{s}$ in all three cases simulated, which corresponds to the output from the side control system

$\omega_{SetSide}$ (all below $150^\circ/\text{s}$). In all three cases, the steady state operating point of the hovercraft is similar to that predicted by (11): at $\omega_{SetFwd} = 300^\circ/\text{s}$ and $\omega_{SetSide} < 150^\circ/\text{s}$, a 1-meter wide corridor leads to $D_{R\infty} = D_{L\infty} = 0.5 \text{ m}$

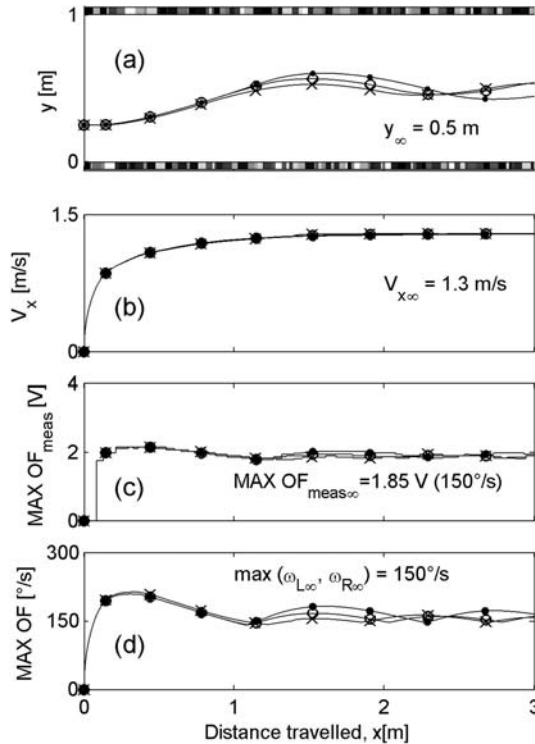


Fig. 8 Automatic centring behaviour occurs whenever the sideways OF set-point $\omega_{SetSide}$ is smaller than half the value of the forward OF set-point ω_{SetFwd} (Marks on trajectories indicate the hovercraft position at 0.3-second intervals). **a** Three simulated trajectories of the hovercraft moving to the right in a straight corridor at a forward OF set-point $\omega_{SetFwd} = 3.28$ V (i.e., $300^\circ/\text{s}$) and various sideways OF set-points (crosses: $\omega_{SetSide} = 1.78$ V ($130^\circ/\text{s}$), open dots: $\omega_{SetSide} = 1.61$ V ($110^\circ/\text{s}$), full dots: $\omega_{SetSide} = 1.36$ V ($90^\circ/\text{s}$)) starting at the initial position $y_0 = 0.25$ m. In all three cases, the hovercraft can be seen to centre between the two walls, oscillating about the midline due to changes in sign in the error signal ε_{Side} (cf. (6)). **b** Forward speed profiles corresponding to the trajectories shown in (a). In the steady state, the forward speed reaches $V_{x\infty} = 1.3$ m/s in the three simulated cases. **c** The maximum value from the two lateral OFs measured $\max(\omega_{Lmeas}, \omega_{Rmeas})$ from the OF sensors corresponding to trajectories shown in (a). In the steady state, this maximum value does not reach the sideways OF set-point $\omega_{SetFwd} = 2.21$ V in the three simulated cases due to the finite corridor width. **d** Maximum value recorded by the two lateral OFs $\max(\omega_L, \omega_R)$ generated by the hovercraft's own motion corresponding to the trajectories shown in (a). In the steady state, the two lateral OFs are equal to $150^\circ/\text{s}$, which is half the value of the forward OF set-point ($300^\circ/\text{s}$)

and $V_{x\infty} = 1.31$ m/s. The maximum value of each lateral OFs can be seen to reach the value $\omega_{SetFwd}/2 = 150^\circ/\text{s}$ for all three values of $\omega_{SetSide} < 150^\circ/\text{s}$ (Fig. 8d), their sum being therefore equal to the *forward OF set-point* $\omega_{SetFwd} = 300^\circ/\text{s}$.

6.2 Automatic response to a “no contrast” zone

Figure 9 shows the effect of the local absence of contrast on one wall. This ‘no contrast zone’ simulates either a true opening in the wall or a gap in the texture. Unable to mea-

sure any OF along the 4-meter long aperture encountered on its left-hand side, the hovercraft can be seen to follow the right wall (Fig. 9a). At the start, we observe the ‘step response’ of the *two OF regulators*: the forward speed increases transiently (Fig. 9b) before reaching a steady state at $V_{x1\infty} = 1$ m/s and $y_{1\infty} = 0.25$ m. From $X = 2$ m to $X = 2.5$ m, the hovercraft is not affected yet by the “no contrast” zone because the left OF sensor holds the last OF measured for another 0.5 s (Fig. 9c). Once this hold time has elapsed: $\omega_{Lmeas} = 0$ and an acceleration phase can be seen to occur transiently (Fig. 9b). This is because the environment is less cluttered, which reduces the sum ($\omega_{Rmeas} + \omega_{Lmeas}$) (Fig. 9c). The forward speed V_x is therefore bound to increase until the maximum forward speed $V_{x2\infty} = 2$ m/s (Sect. 3.2) is reached (Fig. 9b). The steady state operating point of the hovercraft is similar to that predicted by (10b) ($V_{x2\infty} = 2$ m/s and $D_{R2\infty} = y_{2\infty} = 0.5$ m: Fig. 9b, c).

Balancing the two lateral OFs in the experiment described in Fig. 9, however, would have made the robot rush into the opening, since an opening gives rise to virtually zero OF. Some authors have already dealt with this problem in the past and suggested *switching* to wall-following behaviour whenever the mean value of the two lateral OFs becomes larger than a given threshold (Weber et al. 1997) or whenever one of the two lateral OFs is equal to zero (Santos-Victor et al. 1995). Wall-following behaviour was then obtained by controlling the robot’s heading so as to maintain the unilateral OF constant on one side, which means that at a given forward speed, the robot would tend to stay at a ‘pre-specified distance’ from the wall (Santos-Victor et al. 1995; Weber et al. 1997; Zufferey and Floreano 2005). By contrast, we observe the LORA III autopilot leads the robot to perform either *wall-following* or *centring* behaviours without having to switch abruptly from one behaviour to the other.

6.3 Automatic navigation in the case of OF step perturbations introduced by a moving wall

The motion of the right wall is simulated by updating the position of the grey level patterns at each time step. Figure 10a shows the hovercraft’s trajectory when the right wall is moving at a constant speed *in the direction of travel* ($V_p > 0$) over a distance of 3 m (from $X = 3$ m to $X = 6$ m). When the hovercraft enters this nonstationary section, it can be seen to come closer to the moving wall. Figure 11a shows the opposite situation, where the wall is moving *against the direction of travel* ($V_p < 0$). From $X = 3$ m to $X = 6$ m, the hovercraft can be seen to shift away from the moving wall. To explain how these shifts towards or away from the moving wall occur, one must realize that the contrast pattern speed V_p on the right wall is treated by LORA III like an ‘output perturbation’ that affects both loops (see Sect. 4.2).

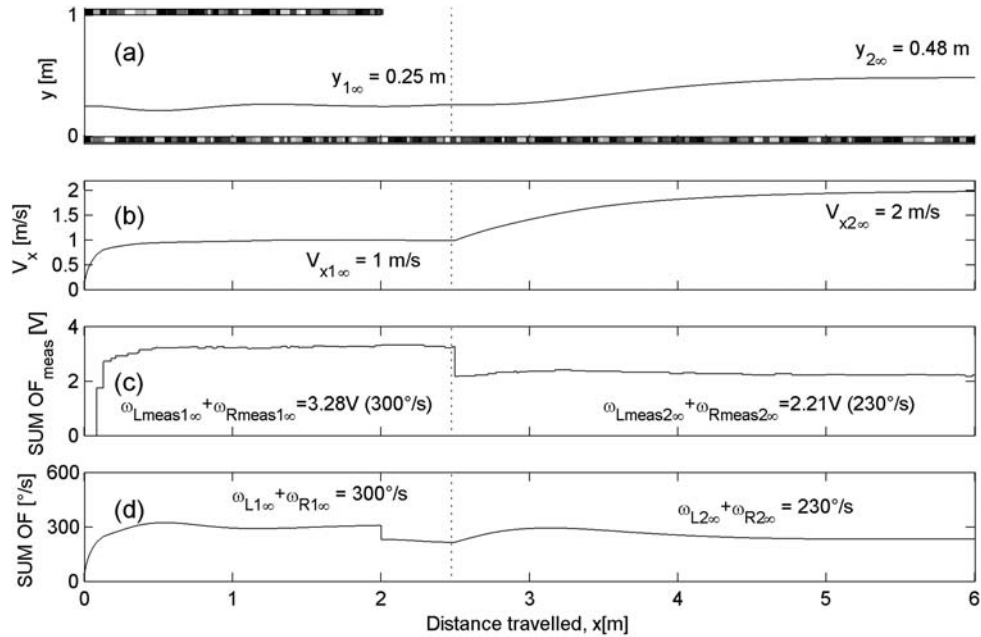


Fig. 9 Automatic reaction to a “no contrast” zone. **a** Simulated trajectory of the hovercraft moving to the right in a straight corridor at a forward OF set-point $\omega_{SetFwd} = 3.28$ V (300°/s) and a sideways OF set-point $\omega_{SetSide} = 2.21$ V (230°/s) starting at the initial position $y_0 = 0.25$ m. The hovercraft is hardly affected by a 4-meter long “no contrast” zone along the left wall. **b** Forward speed profiles corresponding to the trajectories shown in **(a)**. At the start, we observe the step response of the *two OF regulators*: the forward speed increases transiently before reaching a steady state at $V_{x1\infty} = 1$ m/s. As the OF is disturbed by the “no contrast” zone ($\omega_L = 0$), the forward speed V_x

is bound to increase until the maximum forward speed $V_{x2\infty} = 2$ m/s is reached. **c** The sum of the two lateral OFs measured does not reach ω_{SetFwd} due to the saturation of the forward speed, which produces a steady state error in the forward control system. **d** Sum of the two lateral OFs generated by the hovercraft’s own motion corresponding to the trajectories shown in **(a)**. In the steady state, the forward control system does not completely reject the ‘step perturbation’ due to the forward speed saturation. The sum of the OF values reaches the same value as the right OF (230°/s), which corresponds to the sideways OF set-point (230°/s)

In the initial, stationary part of the corridor (Fig. 10a, b, left part), the hovercraft reaches the steady-state operating point ($V_{x1\infty} = 1$ m/s, $y_{1\infty} = 0.25$ m) as in Fig. 7a, b. Later on, from $X = 3$ m to $X = 6$ m, the positive speed of the contrasted patterns ($V_p > 0$) causes a negative OF step perturbation of $-115^\circ/\text{s}$ (Fig. 10d, f). When the speed of the contrasted patterns is negative ($V_p < 0$), we can see that a similar but positive OF step perturbation ($+115^\circ/\text{s}$) is applied to the *autopilot* (Fig. 11d, f). In both cases, the final operating point of the hovercraft ($V_{x2\infty}, y_{2\infty}$) along the moving wall is close to that predicted by (13): at $D = 1$ m, $\omega_{SetFwd} = 300^\circ/\text{s}$ and $\omega_{SetSide} = 230^\circ/\text{s}$, a wall speed of $V_p = +0.5$ m/s gives ($V_{x2\infty} = 1.1$ m/s; $y_{2\infty} = 0.14$ m), whereas *ceteris paribus*, the opposite wall speed ($V_p = -0.5$ m/s) gives ($V_{x2\infty} = 0.82$ m/s; $y_{2\infty} = 0.33$ m). In other words, when a smaller OF is measured by one eye, this is taken to mean that the moving wall is farther away, which causes the hovercraft to accelerate while coming closer to that wall (Fig. 10a, b); conversely when a larger OF is measured, this has the opposite effect (Fig. 11a, b).

These two additional computer-simulated experiments show that the hovercraft remains stable to OF step perturbations and also that LORA III autopilot matches previous

ethological findings obtained on bees in a nonstationary corridor (Kirchner and Srinivasan 1989).

6.4 Automatic deceleration and acceleration in a tapered corridor

The visual environment simulated here is a 6-meter long *tapered* corridor with a 1.24-meter wide entrance and a 0.5-meter wide constriction located midway (Fig. 12a). Its right and left walls are lined with the same random pattern of grey vertical stripes as that used previously (covering a 1-decade contrast range from 4% to 38%, and a 1.5-decade angular frequency range from 0.034 c° to 1.08 c° reading from the longitudinal axis of the corridor). Again, no special steps were taken here to make the two opposite patterns mirror-symmetric.

As shown in Fig. 12b, the hovercraft automatically slows down as it approaches the narrowest section of the tapered corridor and accelerates again when the corridor widens beyond it. The hovercraft therefore negotiates a narrow passage by automatically decelerating (and accelerates once it has passed) the constriction. In Fig. 12a, the hovercraft can be seen to adopt *wall-following behaviour* ($\omega_{SetSide} > \omega_{SetFwd}/2$, see Sect. 4.1). It can be seen from Fig. 12c that

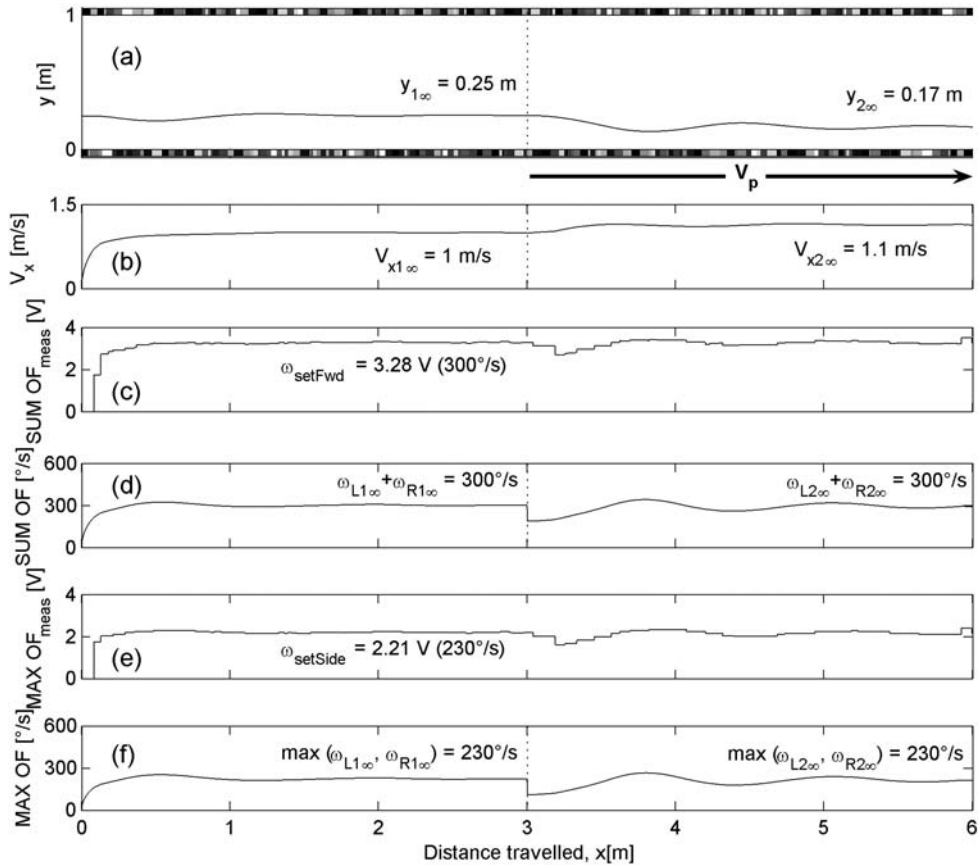


Fig. 10 Automatic reaction to a negative OF step perturbation resulting from a moving wall. The OF perturbation V_p/y_∞ is therefore a negative step of $-115^\circ/\text{s}$. **a** Simulated trajectory of the hovercraft moving to the right in a straight corridor at a forward OF set-point $\omega_{\text{SetFwd}} = 3.28 \text{ V (}300^\circ/\text{s)}$ and a sideways OF set-point $\omega_{\text{SetSide}} = 2.21 \text{ V (}230^\circ/\text{s)}$ from the initial position $y_0 = 0.25 \text{ m}$. From $X = 3 \text{ m}$ to $X = 6 \text{ m}$, the hovercraft is seen to come closer to the right wall that moves at the speed $V_p = +0.5 \text{ m/s}$. **b** Forward speed profiles corresponding to the trajectories shown in **(a)**. At the start, we observe the step response of the two OF regulators: the forward speed increases transiently before reaching a steady state at $V_{x1\infty} = 1 \text{ m/s}$. **c** Sum of the two lateral OFs measured ($\omega_{L\text{meas}} + \omega_{R\text{meas}}$) by the OF sensors corresponding to the trajectories shown in **(a)**. The forward control system in charge of regulating the sum of the two lateral OFs rejects the OF step perturbation caused by the moving wall. During the journey, the sum of the two OFs measured is roughly maintained constant and equal to the

forward OF set-point $\omega_{\text{SetFwd}} = 3.28 \text{ V}$. From $X = 3 \text{ m}$ to $X = 6 \text{ m}$, the relative motion of the right wall reduces the sum of the two lateral OFs measured, and the forward speed V_x increases until the sum of the two lateral OFs measured reaches ω_{SetFwd} . The final operating point of the hovercraft is $V_{x2\infty} = 1.1 \text{ m/s}$ and $y_{2\infty} = 0.17 \text{ m}$. **d** The output of the forward control system, which is the sum of the two lateral OFs generated by the hovercraft's own motion, is regulated at $300^\circ/\text{s}$ in spite of the OF step perturbation resulting from the moving wall. **e** The maximum value of the two lateral OFs measured is regulated at $\omega_{\text{SetSide}} = 2.21 \text{ V}$, shifting the hovercraft toward the moving wall to compensate for its relative motion. **f** The output from the side control system, which is the maximum value of the two lateral OFs generated by the hovercraft's own motion, is maintained approximately constant and equal to $230^\circ/\text{s}$, in spite of the OF step perturbation. In the steady state, the right OF measured reaches the sideways OF ($230^\circ/\text{s}$)

the forward control system strives to keep the sum of the two lateral OFs measured constant and equal to the *forward OF set-point* $\omega_{\text{SetFwd}} = 3.28 \text{ V (}300^\circ/\text{s)}$. Likewise, Fig. 12e shows that the side control system itself strives to keep the maximum value of the two lateral OFs measured equal to the *sideways OF set-point* $\omega_{\text{SetSide}} = 2.21 \text{ V (}230^\circ/\text{s)}$. The forward speed profile along the tapered corridor is particularly instructive (Fig. 12b and Fig. 13d): at all times, the hovercraft's forward speed V_x tends to be proportional to the local corridor width (as predicted in Sect. 4.3).

Plotting the forward speed V_x as a function of the distance travelled x defines a *phase plane* (Fig. 13d), in which

the *time constant* $\tau(\alpha)$ of the visual closed loop in the tapered corridor can be assessed directly (cf. (20)). The *time constant* $\tau(\alpha)$ of the visual closed loop in the tapered corridor depends suitably on the sum (Fig. 13b) of the two lateral OFs: $\text{sum}(\omega_R, \omega_L)$, as well as on the maximum value (Fig. 13c) of the two lateral OFs: $\max(\omega_R, \omega_L)$, which are maintained constant throughout the tapered corridor:

$$\tau(\alpha) = \frac{\text{sum}(\omega_R, \omega_L)}{2 \cdot \tan |\alpha| \cdot \max(\omega_R, \omega_L) \cdot (\text{sum}(\omega_R, \omega_L) - \max(\omega_R, \omega_L))}. \quad (23)$$

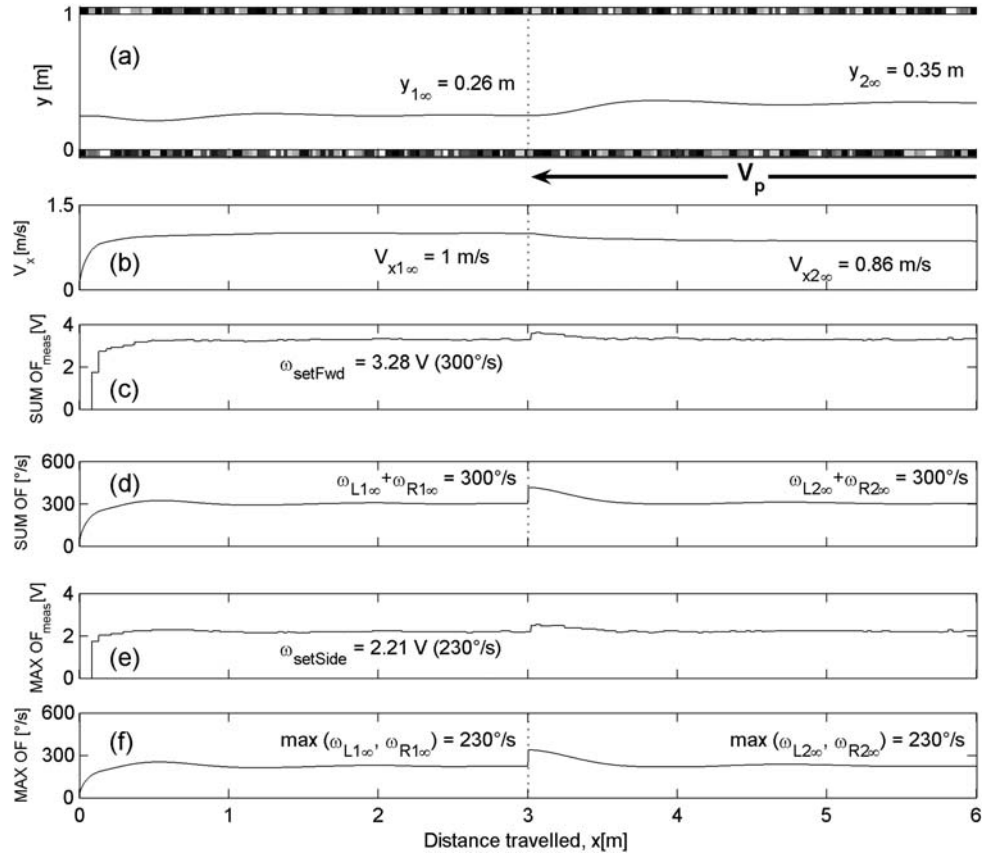


Fig. 11 Automatic reaction to a positive OF step perturbation resulting from a moving wall. The OF perturbation V_p/y_∞ is therefore a positive step of $115^\circ/\text{s}$. **a** Simulated trajectory of the hovercraft moving to the right in a straight corridor at a forward OF set-point $\omega_{SetFwd} = 3.28 \text{ V}$ ($300^\circ/\text{s}$) and a sideways OF set-point $\omega_{SetSide} = 2.21 \text{ V}$ ($230^\circ/\text{s}$) starting from the initial position $y_0 = 0.25 \text{ m}$. From $X = 3 \text{ m}$ to $X = 6 \text{ m}$, the hovercraft shifts its trajectory away from the moving wall (the right one) at a pattern speed $V_p = -0.5 \text{ m/s}$. **b** Forward speed profiles corresponding to the trajectories shown in (a). At the start, we observe the step response of the *two OF regulators*: the forward speed increases transiently before reaching a steady state at $V_{x1\infty} = 1 \text{ m/s}$. **c** Sum of the two lateral OFs measured ($\omega_{Lmeas} + \omega_{Rmeas}$) by the OF sensors corresponding to the trajectories shown in (a). The forward control system in charge of regulating the sum of the two lateral OFs rejects the OF step perturbations resulting from the moving wall. During its journey, the sum of the two OFs measured is maintained approximately con-

stant and equal to the forward OF set-point $\omega_{SetFwd} = 3.28 \text{ V}$. From $X = 3 \text{ m}$ to $X = 6 \text{ m}$, the relative motion of the right wall increases the sum of the two lateral OFs measured, and the forward speed V_x decreases until the sum of the two lateral OFs measured reaches ω_{SetFwd} . The final operating point of the hovercraft is $V_{x2\infty} = 0.86 \text{ m/s}$ and $y_{2\infty} = 0.35 \text{ m}$. **d** The output of the forward control system, which is the sum of the two lateral OFs ($\omega_L + \omega_R$) generated by the hovercraft's own motion happens to be regulated at $230^\circ/\text{s}$ despite the OF step perturbation caused by the moving wall. **e** The maximum value of the two lateral OFs measured is regulated at $\omega_{SetSide} = 2.21 \text{ V}$, thus shifting the hovercraft away from the moving wall to compensate for its relative motion. **f** The output from the side control system, which is the maximum value of the two lateral OFs generated by the hovercraft's own motion, is maintained approximately constant and equal to $230^\circ/\text{s}$ in spite of the OF step perturbation. In the steady state, the right OF measured reaches the sideways OF ($230^\circ/\text{s}$)

The *OF sum* is held virtually constant (at a mean value $\omega_{Lmeas} + \omega_{Rmeas} = 3.51 \text{ V} \equiv 340^\circ/\text{s}$; Figs. 12c, 13b) throughout the converging section of the corridor (tapering angle $\alpha = -7^\circ$). Likewise, the *OF maximum value* is held virtually constant (at a mean value $\omega_{Rmeas} = 2.25 \text{ V} \equiv 240^\circ/\text{s}$; Figs. 12e, 13c). It can be seen from Fig. 13b, c, however that there is a discrepancy between the values attained and the values expected (*OF sum* = $\omega_{SetFwd} = 300^\circ/\text{s}$ and *OF max* = $\omega_{SetSide} = 230^\circ/\text{s}$). The reason for this discrepancy is that the LORA III autopilot entails a ‘following error’.

From the slope of the regression line (equal to -0.305 s^{-1} in Fig. 13d), we can derive the *time constant of the visual closed loop* $\tau_{Conv}(\alpha = -7^\circ) = 1/0.305 = 3.28 \text{ s}$ (Fig. 13e). This value, $\tau_{Conv} = 3.28 \text{ s}$, matches that computed with (23). In the diverging section of the corridor (tapering angle $\alpha = +7^\circ$), the *OF sum* can be seen to be held virtually constant (at a mean value $\omega_{Lmeas} + \omega_{Rmeas} = 3.05 \text{ V} \equiv 280^\circ/\text{s}$; Figs. 12, 13b), and so can the *OF max* (at a mean value $\omega_{Rmeas} = 2.15 \text{ V} \equiv 220^\circ/\text{s}$; Fig. 12e, 13c). Again, a good match can be observed between the *time constant of the visual closed loop* $\tau_{Dive}(\alpha = 7^\circ) = 1/0.202 = 4.96 \text{ s}$ (Fig. 13e) and that computed with (23). The difference be-

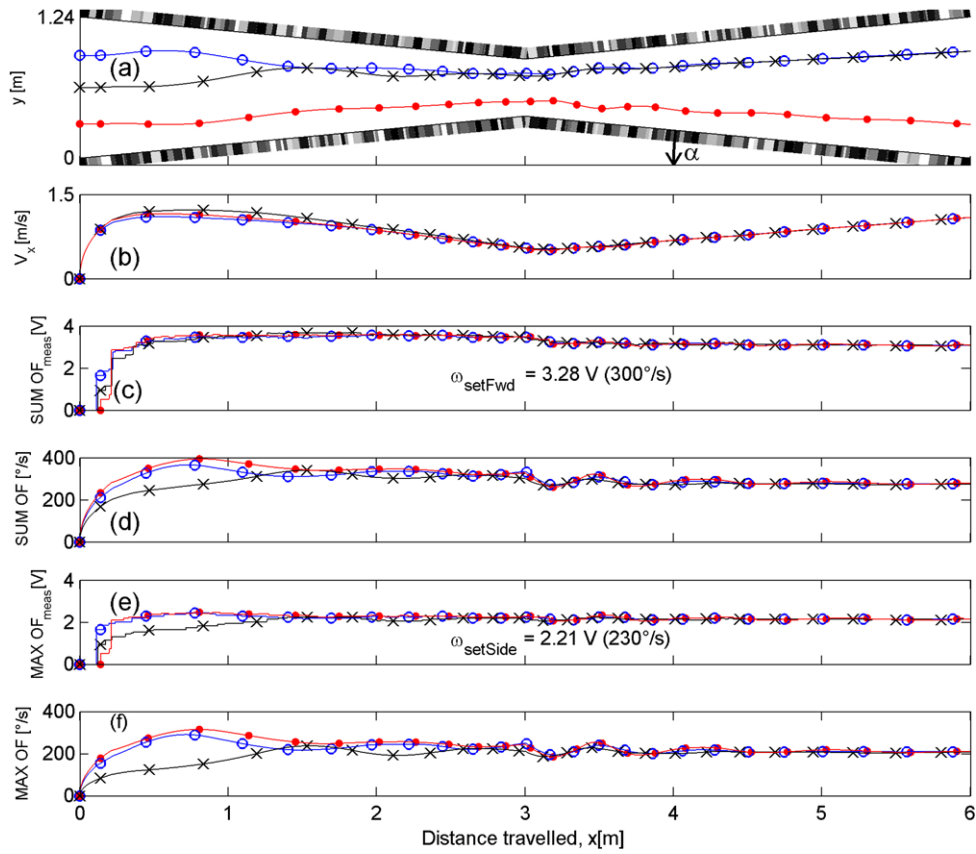


Fig. 12 Automatic deceleration and acceleration of the hovercraft in a tapered corridor in the absence of knowledge on the tapering angle (Marks on trajectories indicate the hovercraft position at 0.3-second intervals). **a** Three simulated trajectories of the hovercraft moving to the right in a tapered corridor (tapering angle $\alpha = 7^\circ$) at a forward OF set-point $\omega_{SetFwd} = 3.28$ V ($300^\circ/\text{s}$) and a sideways OF set-point $\omega_{SetSide} = 2.21$ V ($230^\circ/\text{s}$), starting with different initial ordinates (open dots: $y_0 = 0.90$ m, crosses: $y_0 = 0.60$ m, full dots: $y_0 = 0.30$ m). These trajectories show that the hovercraft automatically slows down when the local corridor width decreases and accelerates again when it widens. **b** Forward speed profiles corresponding to the trajectories shown in **(a)**. The forward speed happens to be a linear function of the distance x travelled, and it is therefore proportional to the local

corridor width D . **c** The forward control system strives at all times to maintain the sum of the two lateral OFs measured constant and equal to ω_{SetFwd} . **d** Sum of the two lateral OFs generated by the hovercraft's own motion (computed with (4) plus (5)) corresponding to the trajectories shown in **(a)**. The forward control system strives to keep the sum of the two lateral OFs measured constant and equal to $300^\circ/\text{s}$. **e** The side control system strives to keep the maximum value of the two lateral OFs measured constant and equal to $\omega_{SetSide} = 2.21$ V ($230^\circ/\text{s}$). **f** Maximum value of the two lateral OFs generated by the hovercraft's own motion (computed with (4) or (5)) corresponding to the trajectories shown in **(a)**. The side control system strives to keep the maximum value of the two lateral OFs constant and equal to $230^\circ/\text{s}$

tween the theoretical value ($\tau(\alpha = 7^\circ) = 4.35$ s computed with (20), and the two experimental values (τ_{Conv} and τ_{Divg}) measured is again due to the ‘following error’ of the LORA III feedback loops.

All in all, these simulation experiments show that the LORA III *dual OF regulator* is able to cope with the major disturbance caused by a tapered corridor, by making the robot decelerate or accelerate appropriately, although it has no detailed information about the local corridor width. Let us recall that the deceleration and acceleration time constant $\tau(\alpha)$ is a monotonic function of the tapering angle α (cf. (20)).

7 Discussion and conclusion

The results of the present computer-simulated experiments show that a hovercraft can navigate safely under visual control along a straight or tapered corridor, and even along a nonstationary corridor, although it is equipped with a really minimalistic visual system (consisting of only 4 pixels forming two *elementary motion detectors*, see Figs. 1, 2). The key to the working of the LORA III autopilot presented here is a pair of *lateral OF regulators* that function in parallel, each controlling its own degree of freedom, with its own OF set-point. One of them controls the vehicle's forward speed, and the other one controls the side speed and hence the vehicle's lateral positioning. The great advantage of this visuomotor control system is that it operates without any need for ex-

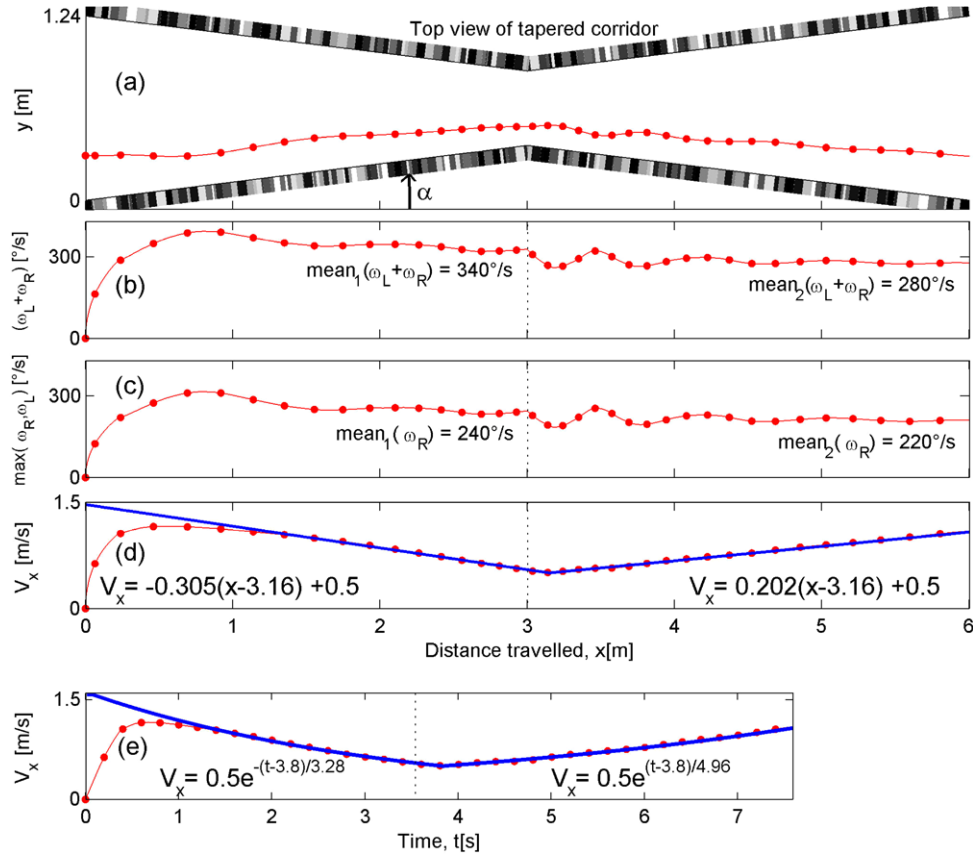


Fig. 13 Forward speed profile in a tapered corridor (tapering angle $\alpha = 7^\circ$) corresponding to the same simulated trajectory as that shown in Fig. 12 (Marks on trajectories indicate the hovercraft position at 0.2-second intervals). **a** Simulated trajectory of the hovercraft moving to the right in a tapered corridor at a forward OF set-point $\omega_{SetFwd} = 3.28$ V (300°/s) and a sideways OF set-point $\omega_{SetSide} = 2.21$ V (230°/s). The LORA III dual OF regulator (Fig. 5) makes the hovercraft automatically slow down when the corridor width decreases and automatically accelerate when the width increases. **b** Sum of the two lateral OFs generated by the hovercraft's own motion (computed with (4) plus (5)) corresponding to the trajectories shown in (a). The forward control system strives to keep the sum of the two lateral OFs measured constant and equal to ω_{SetFwd} (300°/s). **c** Maximum value

of the two lateral OFs generated by the hovercraft's own motion (computed with (4) plus (5)) corresponding to the trajectories shown in (a). The side control system strives to keep the maximum value of the two lateral OFs measured constant and equal to $\omega_{SetSide}$ (230°/s). **d** Phase plane plot of the forward speed V_x as a function of the distance x along the corridor. The forward speed V_x turns out to be a linear function of the distance x . The slope of the linear regression curve (blue line) is equal to the inverse of the forward speed time constant in closed loop $\tau(\alpha)$ (cf. (20)). This time constant in closed loop is equal to 3.28 s (4.96 s) in the converging (or diverging) part of the tapered corridor. **e** The forward speed is an exponential function of time, as expected from the phase plane in (b)

plicit data about speed and distance, and hence without any need for speed sensors or range sensors to control the forward speed and avoid lateral obstacles. Although the hovercraft is completely ‘unaware’ of its own speed, its clearance from the two walls and the width of corridor it is in, it behaves appropriately by automatically adjusting its speed to the environment and automatically maintaining a safe clearance from the walls. The robot navigates on the sole basis of two parameters which are the set-points of the dual OF regulator: a *sideways OF set-point* $\omega_{SetSide}$ and a *forward OF set-point* ω_{SetFwd} , which fully constrain the vehicle's behaviour in a corridor of a given width. By increasing the *forward OF set-point* at a given *sideways OF set-point*, one can change the vehicle's forward speed. By reducing the *sideways OF set-point* at a given *forward OF set-point*, one can induce a

graceful shift from ‘wall-following behaviour’ to ‘centring behaviour’. Centring behaviour occurs as a particular case of wall following behaviour, whenever $\omega_{SetSide} \leq \omega_{SetFwd}/2$.

With its two intertwined feedback loops, the LORA III dual OF regulator therefore provides the vehicle on which it is mounted with both a cruise control system and a lateral anti-collision system, as described below:

- the first *lateral OF regulator* adjusts the hovercraft's side-slip thrust (which determines the side speed V_y , i.e., the sway speed) so as to keep the *maximum* of the two lateral OF equal to the *sideways OF set-point*. In a stationary corridor, the distance from the wall will therefore become proportional to the forward speed V_x that

- is defined in (ii): the faster the hovercraft travels, the further away from the wall it will be.
- (ii) the second *lateral OF regulator* adjusts the forward thrust (which determines the hovercraft's forward speed V_x , *i.e.*, the surge speed) so as to keep the sum of the two (right and left) lateral OFs equal to the *forward OF set-point*. In a stationary corridor, the hovercraft's forward speed V_x becomes proportional to the local corridor width D : the less cluttered the environment is, the faster the hovercraft will travel.

All in all, the two visuo-motor feedback loops automatically yield a ‘safe operating point’ in terms of a groundspeed that is commensurate with the clearance from the walls.

Our control scheme (Fig. 5) accounts remarkably well for the behaviour observed in bees flying along a stationary or nonstationary corridor (Kirchner and Srinivasan 1989), or along a tapered corridor (Srinivasan et al. 1996), despite the minimalistic number of OF sensors with which it is equipped (one on the right, one on the left). The latter authors established that honeybees adopt a *centring behaviour* along a tapered corridor with a tapering angle of $|\alpha| = 15^\circ$. From their Figs. 2A–C, we can figure out that bees were holding the lateral OF on both eyes at approximately $320^\circ/\text{s}$. The control scheme described here (Fig. 5) would then predict that the honeybees were striving to maintain the greater of the two lateral OFs equal to a *sideways OF set-point* $\omega_{SetSide Bee} \approx 320^\circ/\text{s}$ (computed from Fig. 2C data in Srinivasan et al. 1996), while maintaining the sum of the two lateral OFs equal to a *forward OF set-point* $\omega_{SetFwdBee} \approx 640^\circ/\text{s}$ (*centring behaviour* requires $\omega_{SetSide} \leq \omega_{SetFwd}/2$, see Sect. 4.1). It is therefore striking that the slope of the regression line (1.5 s^{-1}) which can be assessed from Fig. 2C in Srinivasan et al. (1996) can be remarkably accurately predicted by the slope (1.5 s^{-1}) obtained from (17b). The simulated control scheme described here (Fig. 5) therefore yields data that are similar to those measured in real flying insects (Kirchner and Srinivasan 1989; Srinivasan et al. 1996; Serres et al. 2007; Ruffier et al. 2007), which suggests that a similar control scheme may well be implemented in the insect nervous system.

The LORA III autopilot can be applied to other types of (holonomic and fully actuated) vehicles such as blimps (*e.g.*, Iida 2001, by adding two *lateral* thrusters), autonomous underwater vehicles (*e.g.*, Smallwood and Whitcomb 2004), and helicopters with counterrotating rotors (in which pitch and roll are uncoupled). Our OF-based autopilot needs to be improved by enlarging its visual field and devising a means of controlling the third degree of freedom (yaw) visually to enable the robot to successfully negotiate more challenging corridors including L-junctions or T-junctions. The additional vision-based control module required for this purpose could be designed by comparing the two frontal-lateral parts of the OF-field, as flies seem to do when they trigger body

saccades (Wagner 1982; Schilstra and van Hateren 1999; Tammero and Dickinson 2002; Zufferey and Floreano 2005; Bermudez i Badia et al. 2007). Implementation of the overall LORA III autopilot on our fully actuated miniature hovercraft (Fig. 1) is now underway.

Insect-based visual systems can yield solutions that require a much smaller number of pixels than those used in the present-day computer-vision systems harnessed to mobile robots. We have described here how a robot can navigate safely in unfamiliar, and even challenging environments such as a tapered corridor with randomly structured patterns on its walls, using a minimalistic number of pixels (only four pixels in fact) without *any metric sensors such as rangefinders or velocimeters*. Combined with a ventral *OF regulator* ensuring ground obstacle avoidance (Ruffier and Franceschini 2003, 2005; Franceschini et al. 2007), the *dual OF regulator* scheme presented here may open the way to lightweight, low-cost visual guidance systems for autonomous vehicle navigation in unfamiliar indoor and outdoor environments. The passive OF sensors and the simple processing system described here are particularly suitable for use with Micro-Air Vehicles (MAVs), in which highly stringent constraints are imposed in terms of the permissible avionic payload and onboard energy resources.

Acknowledgements We grateful to S. Viollet and F. Aubépart for their fruitful comments and suggestions during this research. We thank M. Boyron (electronics engineer), F. Paganucci and Y. Luparini (mechanical engineers) for their expert technical assistance and J. Blanc for revising the English manuscript. We also thank the three anonymous Referees for their valuable comments. This research was supported by CNRS (Life Science and Engineering Science), and by an EU contract (IST/FET—1999-29043).

References

- Argyros, A. A., Tsakiris, D. P., & Groyer, C. (2004). Biomimetic centring behavior for mobile robots with panoramic sensors. In K. Daniilides & N. Papanikopoulos (Eds.). *IEEE robotics and automation magazine: Vol. 11. Special issue on “panoramic robotics* (pp. 21–30).
- Aubépart, F., & Franceschini, N. (2007). Bio-inspired optic flow sensors based on FPGA: Application to micro-air-vehicles. *Journal of Microprocessors and Microsystems*, 31(6), 408–419.
- Baird, E., Srinivasan, M. V., Zhang, S., & Cowling, A. (2005). Visual control of flight speed in honeybees. *Journal of Experimental Biology*, 208, 3895–3905.
- Bermudez i Badia, S., Pyk, P., & Verschure, P. F. M. J. (2007). A fly-locust based neuronal control system applied to an unmanned aerial vehicle: the invertebrate neuronal principles for course stabilization, altitude control and collision avoidance. *The International Journal of Robotics Research*, 26(7), 759–772.
- Blanes, C. (1986). *Appareil visuel élémentaire pour la navigation à vue d'un robot mobile autonome*. M.S. thesis in neurosciences, Neurosciences, Univ. Aix-Marseille II.
- Carelli, R., Soria, C., Nasisi, O., & Freire, E. (2002). Stable AGV corridor navigation with fused vision-based control signals. In *Proceedings of the 28th conference of industrial electronics society* (Vol. 3, pp. 2433–2438).

- Collett, T. S. (1980). Some operating rules for the optomotor system of a hoverfly during voluntary flight. *Journal of Comparative Physiology A*, 138, 271–282.
- Coombs, D., & Roberts, K. (1992). Bee-bot: using peripheral optical flow to avoid obstacles. In *SPIE: Vol. 1825. Intelligent robots and computer vision XI* (pp. 714–721).
- Dev, A., Kröse, B., & Groen, F. (1997). Navigation of a mobile robot on a temporal development of the optic flow. In *Proceedings of the IEEE international conference on intelligent robots and systems (IROS)* (pp. 558–563).
- Duchon, A. P., & Warren, W. H. (1994). Robot navigation from a Gibsonian viewpoint. In *Proceedings of the international conference on systems, man and cybernetics* (pp. 2272–2277), San Antonio, Texas.
- Franceschini, N. (1985). Early processing of colour and motion in a mosaic visual system. *Neuroscience Research*, 2, 17–49.
- Franceschini, N., Blanes, C., & Oufar, L. (1986). *Passive, non-contact optical velocity sensor* (Technical report) (in French), France: ANVAR/DVAR N°51549, Paris.
- Franceschini, N., Riehle, A., & Le Nestour, A. (1989). Directionally selective motion detection by insect neurons. In D. G. Stavenga & R. C. Hardie (Eds.), *Facets of Vision* (pp. 360–390). Berlin: Springer.
- Franceschini, N., Pichon, J. M., & Blanes, C. (1992). From insect vision to robot vision. *Philosophical Transaction of the Royal Society of London B: Biological Sciences*, 337, 283–294.
- Franceschini, N., Ruffier, F., & Serres, J. (2007). A bio-inspired flying robot sheds light on insect piloting abilities. *Current Biology*, 17, 329–335.
- Griffiths, S., Saunders, J., Curtis, A., Barber, B., McLain, T., & Beard, R. (2006). Maximizing miniature aerial vehicles—obstacle and terrain avoidance for MAVs. *IEEE Robotics and Automation Magazine*, 13, 34–43.
- Hrabar, S. E., Corke, P. I., Sukhatme, G. S., Usher, K., & Roberts, J. M. (2005). Combined optic-flow and stereo-based navigation of urban canyons for a UAV. In *Proceedings of the IEEE/RSJ international conference on intelligent robots and systems* (pp. 3309–3316), Edmonton, Canada.
- Humbert, J. S., Murray, R. M., & Dickinson, M. H. (2005). Sensorimotor convergence in visual navigation and flight control systems. In *Proceedings on the 16th IFAC world congress*, Prague, Czech Republic.
- Humbert, J. S., Hypsol, H., & Chinn, M. (2007). Experimental validation of wide-field integration methods for autonomous navigation. In *Proceedings of the IEEE/RSJ international conference on intelligent robots and systems (IROS)*, San Diego, USA.
- Iida, F. (2001). Goal-directed navigation of an autonomous flying robot using biologically inspired cheap vision. In *Proceedings of the 32nd international symposium on robotics, ISR'2001* (pp. 1404–1409).
- Jin, Z., Waydo, S., Wildanger, E. B., Lammers, M., Scholze, H., Foley, P., Held, D., & Murray, R. M. (2004). MVWT-II: the second generation Caltech multi-vehicle wireless testbed. In *Proceedings of the American control conference, ACC'2004* (Vol. 6, pp. 5321–5326).
- Kirchner, W. H., & Srinivasan, M. V. (1989). Freely flying honeybees use image motion to estimate object distance. *Naturwissenschaften*, 76, 281–282.
- Martin, N., & Franceschini, N. (1994). Obstacle avoidance and speed control in a mobile vehicle equipped with a compound eye. In N. Aoki & I. Masaki (Eds.), *Intelligent vehicles* (pp. 381–386). Cambridge: MIT Press.
- Mura, F., & Franceschini, N. (1994). Visual control of altitude and speed in a flying agent. In D. Cliff et al. (Eds.), *From animals to animats III* (pp. 91–99). Cambridge: MIT Press.
- Mura, F., & Franceschini, N. (1996). Obstacle avoidance in a terrestrial mobile robot provided with a scanning retina. In N. Aoki & I. Masaki (Eds.), *Intelligent vehicles II* (pp. 47–52). Cambridge: MIT Press.
- Muratet, L., Doncieux, S., Briere, Y., & Meyer, J.-A. (2005). A contribution to vision-based autonomous helicopter flight in urban environments. *Robotics and Autonomous Systems*, 50(4), 195–209.
- Neumann, T. R., & Bühlhoff, H. H. (2001). Insect inspired visual control of translatory flight. In J. Kelemen & P. Sosik (Eds.), *LNCS/LNBI: Vol. 2159. Proceedings of the 6th European conference on artificial life ECAL 2001* (pp. 627–636). Berlin: Springer.
- Netter, T., & Franceschini, N. (2002). A robotic aircraft that follows terrain using a neuromorphic eye. In *Proceedings of the IEEE intelligent robots and systems (IROS)* (pp. 129–134), Lausanne, Switzerland.
- Pudas, M., Viollet, S., Ruffier, F., Kruusing, A., Amic, S., Leppävuori, S., & Franceschini, N. (2007). A miniature bio-inspired optic flow sensor based on low temperature co-fired ceramics (LTCC) technology. *Sensors and Actuators A*, 133, 88–95.
- Riley, J. R., & Osborne, J. L. (2001). Flight trajectories of foraging insects: observations using harmonic radar. In I. P. Woiwod, D. R. Reynolds, & C. D. Thomas (Eds.), *Insect movement: mechanisms and consequences* (pp. 129–157). CAB International.
- Ruffier, F., & Franceschini, N. (2003). OCTAVE, a bioinspired visuo-motor control system for the guidance of micro-air vehicle. In Rodriguez-Vazquez, Abbott & Carmona (Eds.), *Proceedings of SPIE conf. on bioengineered and bioinspired systems* (Vol. 5119, pp. 1–12), Maspalomas, Spain, May 19–21, Bellingham, USA.
- Ruffier, F., Viollet, S., Amic, S., & Franceschini, N. (2003). Bio-inspired optical flow circuits for the visual guidance of micro-air vehicles. In *Proceedings of the IEEE international symposium on circuits and systems (ISCAS)* (Vol. III, pp. 846–849), Bangkok, Thailand.
- Ruffier, F., & Franceschini, N. (2005). Optic flow regulation: the key to aircraft automatic guidance. *Robotics and Autonomous Systems*, 50(4), 177–194.
- Ruffier, F., Serres, J., Masson, G. P., & Franceschini, N. (2007). A bee in the corridor: regulating the optic flow on one side. In *Proceedings of the 7th meeting of the German neuroscience society—31st Göttingen neurobiology conference*, Göttingen, Germany, Abstract T14-7B.
- Santos-Victor, J., Sandini, G., Curotto, F., & Garibaldi, S. (1995). Divergent stereo in autonomous navigation: from bees to robots. *International Journal of Computer Vision*, 14, 159–177.
- Schilstra, C., & van Hateren, J. H. (1999). Blowfly flight and optic flow. I. Thorax kinematics and flight dynamics. *Journal of Experimental Biology*, 202, 1481–1490.
- Seguchi, H., & Ohtsuka, T. (2003). Nonlinear receding horizon control of an underactuated hovercraft. *International Journal of Robust and Nonlinear Control*, 13, 381–398.
- Serres, J., Ruffier, F., & Franceschini, N. (2005). Biomimetic visual navigation in a corridor: to centre or not to centre? In *Proceedings of international mediterranean modeling multiconference*, (pp. 91–97), Marseilles, France.
- Serres, J., Ruffier, F., Viollet, S., & Franceschini, N. (2006a). Toward optic flow regulation for wall-following and centring behaviours. *International Journal of Advanced Robotic Systems*, 3, 147–154.
- Serres, J., Ruffier, F., & Franceschini, N. (2006b). Two optic flow regulators for speed control and obstacle avoidance. In *Proceedings of the first IEEE international conference on biomedical robotics and biomechatronics (BIOROB)* (pp. 750–757), Pisa, Italy.
- Serres, J., Ruffier, F., Masson, G. P., & Franceschini, N. (2007). A bee in the corridor: centring or wall-following? In *Proceedings of the 7th meeting of the German neuroscience society—31st Göttingen neurobiology conference*, Göttingen, Germany, Abstract T14-8B.
- Smallwood, D. A., & Whitcomb, L. L. (2004). Model-based dynamic positioning of underwater robotic vehicles: theory and experiment. *IEEE Journal of Oceanic Engineering*, 29, 169–186.

- Srinivasan, M. V., Zhang, S. W., Lehrer, M., & Collett, T. S. (1996). Honeybee navigation. *en route* to the goal: visual flight control and odometry. *Journal of Experimental Biology*, 199, 237–244.
- Srinivasan, M. V., Chahl, J. S., Weber, K., Venkatesh, S., Nagle, M. G., & Zhang, S. W. (1999). Robot navigation inspired by principles of insect vision. *Robotics and Autonomous Systems*, 26, 203–216.
- Tammero, L. F., & Dickinson, M. H. (2002). The influence of visual landscape on the free flight behavior of the fruit fly *Drosophila melanogaster*. *Journal of Experimental Biology*, 205, 327–343.
- Viollet, S., & Franceschini, N. (1999). Visual servo system based on a biologically-inspired scanning sensor. In *Proceedings of SPIE conf. on sensor fusion and decentralized control on robotics II* (Vol. 3839, pp. 144–155), Boston, USA.
- Viollet, S., & Franceschini, N. (2005). A high speed gaze control system based on a vestibulo-ocular reflex. *Robotics and Autonomous Systems*, 50(4), 147–161.
- von Frisch, K. (1948). Gelöste und ungelöste Rätsel der Bienensprache. *Naturwissenschaften*, 35, 38–43.
- Wagner, H. (1982). Flow-field variables trigger landing in flies. *Nature*, 297, 147–148.
- Wagner, H. (1986). Flight performance and visual control of flight in the free-flying house fly (*Musca domestica* L.). I: Organization of the flight motor. *Philosophical Transactions of the Royal Society of London B*, 312, 527–551.
- Weber, K., Venkatesh, S., & Srinivasan, M. V. (1997). Insect inspired behaviours for the autonomous control of mobile robots. In M. V. Srinivasan & S. Venkatesh (Eds.), *From living eyes to seeing machines* (pp. 226–248). Oxford: Oxford University Press.
- Zufferey, J.-C., & Floreano, D. (2005). Toward 30-gram autonomous indoor aircraft: vision-based obstacle avoidance and altitude control. In *Proceedings of the IEEE international conference on robotics and automation (ICRA)* (pp. 2594–2599), Barcelona, Spain.



J. Serres was born in Aix-en-Provence, France. He obtained an *Agréation* in Applied Physics (a high-level competitive examination for recruiting teachers in France) at the Ecole Normale Supérieure, Cachan, France, in 2002. He took a Master's degree in Medical Imaging from Paris XI University (Orsay) and a Master's degree in Electronics, Electrotechnics, and Automatic Control Engineering from Paris XI University and the Ecole Normale Supérieure (ENS Cachan), Orsay, France, in 2003. In 2003, he joined the Biorobotics

Lab at the Movement and Perception Institute, C.N.R.S. and University of the Mediterranean, Marseille, France, as a Ph.D. student.



D. Dray was born in Marseille, France. He obtained an engineering degree in Mechanics and Computer Science at the Ecole Nationale Supérieure des Arts et Métiers (ENSA), Aix-en-Provence, France, and an engineering degree in Automatic Control Engineering and Signal Processing at the Ecole Supérieure d'Électricité (SUPELEC), Gif-sur-Yvette, France, in 2006. In 2006, he was Master's student at Biorobotics Lab at the Movement and Perception Institute, C.N.R.S. and University of the Mediterranean, Marseille, France.



F. Ruffier was born in Villefranche-sur-Saône, France. He obtained an engineering degree in Computer Science, Electronics and Control Theory from the National Polytechnic Institute, Grenoble. He spent one year as an exchange student in the Automatic Control department in Lund, Sweden. In 2000, he joined the Biorobotics Lab at the C.N.R.S. in Marseille, France and obtained his Ph.D. degree at the National Polytechnic Institute, Grenoble (INP Grenoble) in September 2004. His present position is C.N.R.S. Staff Researcher at the Biorobotics Lab at the Movement and Perception Institute, C.N.R.S. and University of the Mediterranean, Marseille, France.



N. Franceschini was born in Mâcon, France. He graduated in Electronics and Control Theory at the National Polytechnic Institute, Grenoble, and then studied Biophysics, Neurophysiology, and Behavioural Science at the University and Max-Planck Institute for Biological Cybernetics, Tübingen (Germany). He received the doctor's degree in Physics at the University of Grenoble in 1972 and spent nine years as a researcher at the Max-Planck Institute. He then settled down in Marseille, where he built up a Neurocybernetics Research Group at the National Center for Scientific Research (C.N.R.S.). His present position is C.N.R.S Research Director and Head of the Biorobotics Lab at the Movement and Perception Institute, C.N.R.S. and University of the Mediterranean, Marseille, France.